

CHARACTERIZING THE CLUSTER LENS POPULATION

JOSEPH F. HENNAWI^{1,2,3}, NEAL DALAL^{1,4}, PAUL BODE³, JEREMIAH P. OSTRICKER³

Draft version November 5, 2018

ABSTRACT

We present a detailed investigation into which properties of cold dark matter halos make them effective strong gravitational lenses. The cross sections for giant arc formation of 878 clusters from a high-resolution N-body simulation of the Λ CDM cosmology are measured by ray tracing through 13,594 unique projections. We measure concentrations, axis ratios, orientations, and the amount of substructure of each cluster, and compare the lensing weighted distribution of each quantity to that of the cluster population as a whole. We find that NFW profiles provide just as good a fit to lensing clusters as they do to the total cluster population; however, the concentrations of lensing clusters are on average 34% larger than the typical cluster in the Universe. Despite this bias, the anomalously high concentrations of lensing clusters ($c > 14$) recently measured by several groups from combined strong and weak lensing analyses (Kneib et al. 2003; Gavazzi et al. 2003; Broadhurst et al. 2005b), appear to be inconsistent with the concentration distribution in our simulations, which predict $< 2\%$ of lensing clusters should have concentrations this high. No correlation is found between strong lensing cross section and the amount of substructure, indicating that the population of cluster lenses is no more relaxed or disturbed than typical clusters in the Universe. Lensing clusters tend to have their principal axis aligned with the line of sight: the median angle is $|\cos \theta| = 0.67$. We introduce several different types of simplified dark matter halos, and use them to isolate which properties of CDM clusters make them effective gravitational lenses. Projections of halo substructure onto small radii and the large scale mass distribution of clusters do not significantly influence strong lensing cross sections. The abundance of giant arcs is primarily determined by the mass distribution within an average overdensity of $\sim 10,000$. The clumpy cores of dark matter halos result in $\sim 25 - 60\%$ more giant arcs than smooth ellipsoids of the same total mass. A multiple lens plane ray tracing algorithm is used to show that projections of large scale structure increase strong lensing cross sections by a modest amount $\lesssim 7\%$. We revisit the question of whether there is an excess of giant arcs detected for high redshift clusters in the Red-Sequence Cluster Survey (Gladders et al. 2003) and find that the number of high redshift ($z \gtrsim 0.6$) lensing clusters is in good agreement with Λ CDM, although our simulations predict more low redshift ($z \lesssim 0.6$) lensing clusters than were observed.

Subject headings: dark matter – galaxies: clusters: cosmology: theory – methods: numerical – clusters: general – large scale structure of the universe – gravitational lensing

1. INTRODUCTION

Strong gravitational lensing by clusters of galaxies provides a unique laboratory for studying the small scale dark matter distribution of the largest collapsed structures in the Universe. Because strong lensing directly probes the gravitational potential, it is free from the assumptions which plague other techniques which probe the mass distribution on comparable scales. For example, dynamical measures (Natarajan & Kneib 1996; Kelson et al. 2002) assume that dark halos are virialized systems and models of the X-ray temperature profile of the intracluster medium (e.g. Arabadjis, Bautz, & Garmire 2002; Ettori, Fabian, Allen, & Johnstone 2002; Lewis, Buote, & Stocke 2003) typically assume hydrostatic equilibrium.

Upcoming X-ray (Romer et al. 2001; Ebeling et al. 2001) Sunyaev-Zeldovich (Carlstrom, Holder, & Reese 2002; Kosowsky 2003; Schwan et al. 2003), and opti-

cal (Gladders & Yee 2004) cluster searches will dramatically increase the number of clusters of galaxies known. Deep follow up imaging of these clusters will discover hundreds of new giant arcs. Such statistical samples of arcs will allow measurement of the giant arc abundance as a function of cluster redshift, the radial distributions of arcs from the cluster center, and the distribution of relative angles between arcs in multi-arc systems. Comparisons of these quantities to expectations from ray tracing simulations of clusters in a Λ CDM cosmology have already been carried out (Bartelmann et al. 1998; Wambsganss et al. 2004a; Dalal, Holder, & Hennaui 2004; Ho & White 2004; Li et al. 2005) using small samples of ~ 20 known arcs (see Sand et al. 2005, for a recent compilation).

Armed with future statistical samples, we will be able to measure the distributions of cluster lens properties, in addition to the simple ‘one point’ statistics of the arcs. Detailed modeling of image positions in cluster lenses can determine a set of best fit parameters which describe the distribution of dark matter in each cluster lens (e.g. Tyson, Kochanski, & dell’Antonio 1998; Smith et al. 2001; Sand et al. 2004; Broadhurst et al. 2005a), and even stronger constraints can be obtained when strong lensing information is combined with larger

¹ Hubble Fellow

² Department of Astronomy, University of California Berkeley, Berkeley, CA 94720

³ Princeton University Observatory, Princeton, NJ 08544

⁴ Institute for Advanced Study, Einstein Drive, Princeton, NJ 08540

scale weak lensing measurements (Kneib et al. 2003; Gavazzi et al. 2003; Broadhurst et al. 2005b). These parameters might include the slope of the mass profile, its concentration, or the projected ellipticity of the cluster. A comparison of the observed distribution of these parameters to the expected structures from cosmological simulations of a Λ CDM Universe will provide a strict test of our current theory of dark matter and structure formation.

In this context, the questions naturally arise: Do strong lensing selected clusters constitute a fair sample of clusters in the Universe? Do biases exist with respect to halo concentration, triaxiality, preferential alignment, or the amount mass in substructure? Clearly, these biases must be taken into account before a comparison can be made between the observed distribution of cluster lens properties and the properties of numerically simulated clusters. Additionally, by comparing the distribution of lensing cluster properties to the cluster population as a whole, we can hope to gain insights and intuition about what makes a CDM cluster an effective strong lens.

In this paper we statistically characterize the properties of the cluster lens population. Using the ray tracing technique discussed Dalal, Holder, & Hennawi (2004, henceforth DHH), we compute the lensing cross sections of a large sample of clusters from a cosmological N-body simulation. We measure the properties of each cluster and compare the lensing weighted distribution of cluster properties to the cluster population as a whole. We also attempt to isolate which properties of CDM clusters make them effective gravitational lenses. In this context we introduce ‘Analog Halos,’ which are simplified dark matter halos which retain one or more of the properties of the original simulated clusters. As an aside, we also quantify the effect of projections of large scale structure between the source plane and the observer on the abundance of giant arcs. Armed with lensing cross sections for clusters in a large simulation volume, we revisit the question of whether there is an excess of giant arcs detected for high redshift clusters in the Red-Sequence Cluster Survey (RCS) (Gladders et al. 2003). We were unable to answer this question definitively in DHH because the cosmological volume simulated in that study was too small (see also Wambsganss et al. 2004a).

The cosmological N-body simulation and our methodology for measuring the cluster parameters and quantifying substructure are described in § 2. We review the ray tracing algorithm in § 3 and investigate the effect of additional matter in the light cone in § 4. In § 5, we introduce the ‘Analog Halos’ and examine which properties of CDM halos make them effective gravitational lenses. We compare the statistical properties of cluster lenses to the total cluster population in § 6. The abundance of giant arcs in the RCS is revisited in § 7, and we summarize and conclude in § 8.

2. SIMULATED CLUSTERS

In this section, we describe the simulated clusters which are the input to our ray tracing algorithm. For the analysis in § 5 and § 6 we will require various properties of clusters, such as triaxiality, the amount of substructure, and cluster concentration both in three dimensions and for two dimensional projections. First we describe the N-body simulations and how the clusters were identified,

then we describe how cluster properties were measured.

2.1. N-body simulations

In order to simulate the strong lensing effects of a Universe filled with dark matter, we used clusters drawn from a cosmological N-body simulation. The simulation was performed with the Tree-Particle-Mesh (TPM) code of Bode & Ostriker (2003). TPM uses the Particle-Mesh method for long-range forces and a tree code for sub-grid resolution; individual isolated, overdense regions are each treated as a separate tree, thus ensuring efficient use of parallel computers. The following cosmological parameters were used: matter content $\Omega_M = 0.3$, cosmological constant $\Omega_\Lambda = 0.7$, Hubble constant $H_0 = 70 \text{ km s}^{-1} \text{ Mpc}^{-1}$, linear amplitude of mass fluctuations $\sigma_8 = 0.95$, and primordial power spectral index $n_s = 1$. These parameters are consistent (within 1σ) of the WMAP derived cosmological parameters (Spergel et al. 2003). The simulation volume is a periodic cube with comoving side length of $L = 320 h^{-1} \text{ Mpc}$ containing $N = 1024^3$ particles, so the particle mass is $m_p = 2.54 \times 10^9 h^{-1} M_\odot$. The cubic spline softening length was set to $\epsilon = 3.2 h^{-1} \text{ kpc}$. The small softening length, small particle mass, and large volume make this simulation ideal for studying strong lensing by clusters; this simulation was previously analyzed by Wambsganss et al. (2004a,b). We used outputs at seven different ‘snapshots’, spaced a comoving length L apart and covering the range of redshifts over which the critical density is low enough to produce an appreciable amount of strong lensing. These redshifts are $z = 0.17, 0.29, 0.41, 0.55, 0.70, 0.87, 1.05, 1.26$, and 1.49 .

A “friends-of-friends” (FOF) group finder (Davis et al. 1985) with the canonical linking length of $b = 0.2$ was applied to each particle distribution to identify cluster size dark matter halos. For each cluster with a FOF group mass above $M_{\text{FOF}} \geq 10^{14} h^{-1} M_\odot$, all the particles within a $5 h^{-1} \text{ Mpc}$ sphere about the center of mass were dumped to separate files and used as inputs to our ray tracing code.

2.2. NFW Profile Parameters

For each cluster identified by FOF, the gravitational potential was computed and the center of the cluster was defined to be the most bound particle in the $5 h^{-1} \text{ Mpc}$ particle dump. The radial mass profile of the cluster about this center was calculated, and the virial radius was defined as the radius of the innermost particle at which the average density interior to it was greater than or equal to $\Delta_{\text{vir}}(z)$ times the cosmic *mean* matter density where the virial overdensity is $\Delta_{\text{vir}} \approx \frac{18\pi^2 + 82x - 39x^2}{1+x}$ (Bryan & Norman 1998), with $x \equiv \Omega_m(z) - 1$.

We computed the number of particles in 50 logarithmically spaced radial bins between the 100th particle from the cluster center and the virial radius. The smallest radial bin was placed at the position of the 100th particle because this roughly defines the scale at which the mass distribution is unaffected by two body relaxation effects (Power et al. 2003). This scale exceeds the softening length for all of the clusters we considered and provides a stricter limit on the scales we resolved.

We then fit the number of particles in each bin dN_i to the *number profile* corresponding to the universal density

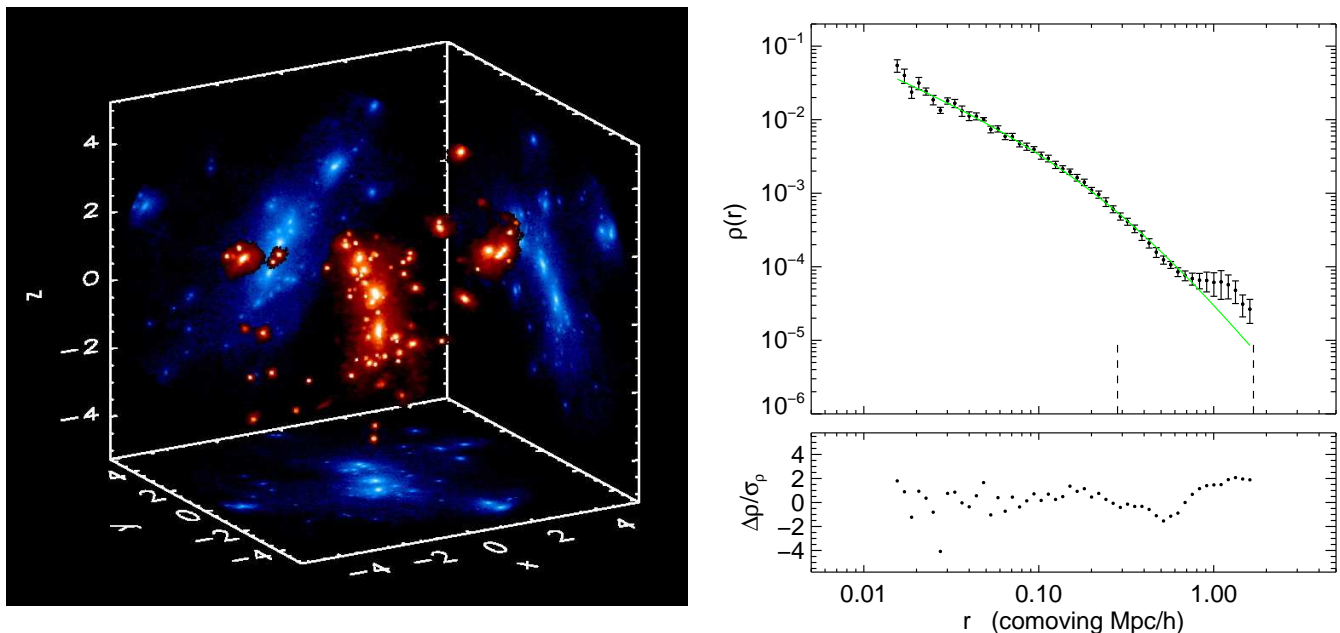


FIG. 1.— Example of a cluster with a large amount of substructure inside the virial radius. *Left:* Three dimensional density distribution of the cluster. Surface density projections on each coordinate plane are also shown to aid visualization. The spatial axes are in units of comoving h^{-1} Mpc and both density (2-d and 3-d) color maps are logarithmically stretched. *Right:* Radial density profile (points) and best fit NFW profile fit (solid green line), which has a reduced $\chi^2 = 1.28$. The y-axis has units of $h^{-1} \text{ M}_{\odot}/\text{pc}^3$. The inner and outer dashed vertical lines indicate the locations of the scale radius and virial radius for the NFW fit, respectively. The lower panel plots the ratio of $\Delta\rho$, which is the difference between the profile and the fit, to σ_{ρ} , the bootstrapped density variance, for each radial bin. The bootstrapped variances properly down weight the bump in the outer radial bins caused by the massive substructures. Had we used the Poisson errors alone the radial bump would have had a catastrophic effect on the fit because $1/\sqrt{N}$ is very small for these outer bins.

profile of Navarro, Frenk, & White (1997) (henceforth NFW). The number of particles in each bin $dN_i \sim r^2 \rho dr$ is much less noisy than the density and furthermore, it is dN_i which should obey Poisson statistics if counting errors are the only source of noise in each measurement, allowing us to assign sensible errors (see discussion below).

Thus we fit the quantity

$$dN_i(r_s, M_C) = M_C [A(x_i) - A(x_{i-1})] \quad (1)$$

for the two parameters M_C and r_s , where

$$A(x) \equiv \ln(1+x) - \frac{x}{1+x}. \quad (2)$$

and $x = r/r_s$. In terms of the familiar NFW parameters $M_C = 4\pi\rho_s r_s^3/m_p$, but we opt to fit for M_C because the profile is linear in this quantity.

The parameters are determined by minimizing the reduced χ^2 penalty function

$$\chi^2 = \frac{1}{50} \sum_{i=1}^{50} \frac{[dN_i - dN_i(r_s, M_C)]^2}{\sigma_i^2}. \quad (3)$$

Our computation of the variance for each logarithmic bin, σ_i^2 , warrants further discussion. The deviations between our simulated clusters and an NFW profile can be caused by both counting errors, described by Poisson statistics, and massive substructures or asymmetries in the cluster. Without taking the latter source of error into account, a bump in the radial profile of a halo will have a catastrophic effect on the NFW fit if it is in the outer region of the halo, because the formal Poisson errors for these radial bins will be very small. Previous

workers have dealt with this problem by removing these substructures from the halo (e.g. Jing & Suto 2002) or truncating the profile and the fit wherever these bumps occur (e.g. Bullock et al. 2001). However, in the context of strong lensing, neither of these approaches is appropriate. We wish to measure a three dimensional profile which is as closely related as possible to the two dimensional surface density profile probed by strong lensing observations. Strong lensing is sensitive to the total projected mass, and since it is not possible to remove or truncate substructures observationally we opt not to do so in the simulations either.

Instead, we define a modified variance which incorporates halo asymmetry but which reduces to the Poisson variance for a spherically symmetric halo. Each radial bin is divided into 12 equal area sectors using Healpix⁵, and we estimate the variance via a ‘bootstrap’

$$\sigma_i^2 \equiv \frac{n_{\text{pix}}}{n_{\text{pix}} - 1} \sum_{j=1}^{n_{\text{pix}}} \left(dn_{ij} - \frac{dN_i}{n_{\text{pix}}} \right)^2, \quad (4)$$

where $n_{\text{pix}} = 12$ is the number of Healpix sectors and dn_{ij} is the number of particles in the i th radial bin which land in angular sector j .

The right panel of Figure 1 compares the measured density profile to the best fit NFW profile⁶, for a cluster from our simulation which is depicted in the left panel. The massive substructure interior to the virial radius

⁵ <http://www.eso.org/science/healpix>

⁶ Although we fit the number profiles using dN_i and σ_i , we plot density profiles $\rho(r)$ and corresponding propagated errors σ_{ρ} for the sake of visualization.

causes a bump in the radial density profile, however, the bootstrapped errors correctly down weight these points and minimize their influence on the fit.

The distribution of the reduced χ^2 for the 878 clusters in our fiducial snapshot is displayed in Figure 6. The fact that median value of this distribution is near unity gives us confidence that the NFW profile is providing a good fit to our simulated clusters and our bootstrapped σ_i are accurately describing the Poisson errors as well as the deviations from symmetry.

Once M_C and r_s are determined, all the NFW parameters r_s , ρ_s , c_{vir} , r_{vir} and M_{vir} can be determined from simple algebraic relations. Although the NFW fit determines the virial mass of the cluster, we instead adopt the non-parametric virial mass given by the mass interior to the virial radius defined by the overdensity criterion Δ_{vir} .

We also perform fits of the surface mass density to a two dimensional projected NFW profile, for various projections through the mass distribution of each cluster. These two dimensional fits are of interest because the projected mass distribution is the quantity accessible to observations of strong lensing. We repeat the fitting procedure described above for surface mass density by computing the azimuthally averaged radial profile in 50 logarithmically spaced bins between 0.02 and $2 h^{-1}$ Mpc. The same bootstrapping procedure (eqn. 4) is used to compute the errors, where we use 20 azimuthal bins to estimate the error for each radial bin. We minimize the χ^2 of a fit to an analytical expression for the projected NFW profile (Bartelmann 1996; Wright & Brainerd 2000). Note that this formula for the projected NFW profile assumes the profile extends to infinity, which results in a slight bias of 6% (see § 6.3) in the concentrations measured. For the sake of simplicity, we use this analytical form rather than fitting to the exact numerical expression for a projected truncated NFW. This small bias does not have a significant effect on our conclusions.

2.3. Substructure

Although complicated algorithms exist to identify substructures in N-body simulations (see e.g. Kravtsov et al. 2003; De Lucia et al. 2004; Weller, Ostriker, & Bode 2004; Gill, Knebe, & Gibson 2004), for our purposes we are only interested in identifying substructures massive enough to influence the strong lensing cross sections of massive clusters, for which even a very simple procedure will suffice. In addition, there is no need to use velocity information to unbind particles as is done in other algorithms since the energy of the matter distribution is irrelevant to its lensing effect. To this end, we identify substructures by rerunning the FOF algorithm on the particles in each cluster dump, but with a smaller linking length of $b = 0.05$. This causes a cluster halo to fragment into one or more dense subhalos. The most massive subhalo will be centered on the potential minimum or center of the cluster, and we designate this as the cluster core. We define as a substructure any additional subhalos (besides the most massive) identified by the FOF algorithm with a mass $M > 10^{12} h^{-1} M_\odot$. This is safely larger than the smallest subhalo resolved by our particle mass $\sim 100 m_p = 2.5 \times 10^{11} h^{-1} M_\odot$.

A linking length $b = 0.05$ groups particles within an isodensity contour of $\sim 4,000$ times the background den-

sity (Lacey & Cole 1994). For an NFW cluster, the smaller linking length truncates the cluster at a radius $\sim r_{10,000}$, where the average overdensity is $\sim 10,000$ times the mean density. For, $M_{\text{vir}} \sim 5 \times 10^{14} h^{-1} M_\odot$, $c_{\text{vir}} = 6$, and $z = 0.4$, $r_{10,000} \sim 300 h^{-1}$ kpc (comoving), which projects to an angular separation of $\sim 1'$.

We define three different statistics which quantify the amount of substructure in a cluster. Two of the three can be written as

$$M_{\text{sub}} \equiv \frac{1}{M_{\text{norm}}} \sum_{i=2}^{N_{\text{sub}}} M_i, \quad (5)$$

where M_i refers to the mass of the i^{th} subhalo, M_{norm} is a normalizing mass, and the sum extends over all substructures enclosed within the virial radius of the halo. Note that the sum excludes subhalo $i = 1$, which as noted above corresponds to the cluster core.

We explore two different normalization masses $M_{\text{norm}} = M_{\text{core}}$ and $M_{\text{norm}} = M_{\text{vir}}$, corresponding to the two statistics $M_{\text{sub-core}}$ and $M_{\text{sub-vir}}$, respectively. The statistic $M_{\text{sub-core}}$ is normalized by the mass of the dense core which is the mass relevant to lensing. This could be biased low for lensing clusters since they might have more massive cores which is why we also consider $M_{\text{sub-vir}}$. Our third substructure statistic is $M_{\text{sub-2}} = M_2/M_{\text{vir}}$, where M_2 is the second most massive sub-halo. This statistic provides a measure of the binarity of the cluster, and is less sensitive to lower mass halos which may dominate the total mass in substructure because they are more abundant.

2.4. Triaxiality

Previous work has shown that for CDM halos, the degree of triaxiality increases (i.e., the axis ratios decrease) toward the center (Barnes & Efstathiou 1987; Warren et al. 1992; Jing & Suto 2002; Schulz et al. 2005). For our purposes, we are interested in the triaxiality of the mass within the dense core which is primarily responsible for the strong lensing. As mentioned in the previous section, we identify the most massive subhalo selected by the FOF algorithm using a smaller linking length with the cluster core. We compute the principal axes and axis ratios by diagonalizing the normalized moment of inertia tensor for the particles which are linked into this core subhalo

$$\mathbf{Q} = \frac{1}{N_{\text{core}}} \sum_i^{N_{\text{core}}} \mathbf{r}_i \otimes \mathbf{r}_i, \quad (6)$$

where N_{core} is the number of particles grouped into the core subhalo. If $a^2 > b^2 > c^2$ are the principal components of \mathbf{Q} , we compute the axis ratios $q_2 \equiv b/a$ and $q_3 \equiv c/a$ for each cluster. The eigenvectors of \mathbf{Q} give the orientation of the principal axes \mathbf{V}_a , \mathbf{V}_b , \mathbf{V}_c . Note that by restricting attention only to particles which lie in the FOF group, we are computing the axis ratios of the particles within an isodensity contour, similar to the approach of Jing & Suto (2002). Other workers have computed the axis ratios of particles within an ellipsoid (Barnes & Efstathiou 1987; Warren et al. 1992) defined by an iterative procedure, but these iterations are not guaranteed to converge (Jing & Suto 2002; Schulz et al. 2005) which is why opt for the method used here.

3. STRONG LENSING CALCULATION

We compute the strong lensing properties of our simulated clusters using ray-tracing; cross sections and arc statistics are determined via Monte Carlo integration over the background source plane. We refer the reader to DHH for details of the ray tracing and the Monte Carlo calculation. The ray trace and Monte Carlo are repeated for each projection through the cluster and for each source plane considered. We ray trace five source planes at $z_s = 1.0, 1.5, 2.0, 3.0$, and 4.0 . The number counts of background galaxies are collapsed into five source redshift bins centered on these source planes given by the intervals $[0.75, 1.25]$, $[1.25, 1.75]$, $[1.75, 2.5]$, $[2.5, 3.5]$, and $[3.5, 6.0]$, respectively. Because the critical density for strong lensing is a slowly varying function of source redshift, this binning should not introduce significant errors in our calculation. Given the cross sections for each source plane and the number counts of background galaxies in each bin, the number of giant arcs behind each cluster orientation can be computed as a function of limiting magnitude or surface brightness.

DHH and Ho & White (2004) found that the lensing cross section for a single cluster varies enormously as a function of orientation (see Figure 3 of DHH). A factor of ~ 20 spread in lensing cross section was not uncommon and the histogram of cross sections for different orientations was quite skewed. To compute reliable mean cross sections for a cluster, we must thus average over many projections to appropriately sample the distribution of cross sections. This orientation averaging is most important for the rarest, most massive clusters in the simulation volume that dominate the total lensing optical depth. We computed mean lensing cross sections by averaging over 125 orientations for all clusters with $M_{\text{FOF}} \geq 10^{14.7} h^{-1} M_\odot$, 31 orientations for clusters in the mass interval $10^{14.3} h^{-1} M_\odot \leq M_{\text{FOF}} < 10^{14.7} h^{-1} M_\odot$, and 3 orientations for all clusters in the range $10^{14} h^{-1} M_\odot \leq M_{\text{FOF}} < 10^{14.3} h^{-1} M_\odot$.

Given the cross sections for each cluster orientation, the total number of arcs caused by the clusters in the snapshot at redshift z_j

$$N_j(> \theta) = \sum_k \Omega n_k \frac{V_j}{L^3} \sum_i^{N_{\text{clusters}}} \bar{\sigma}_{ijk}(> \theta). \quad (7)$$

Here $\bar{\sigma}_{ijk}(> \theta)$ is the orientation averaged cross section for forming giant arcs with angular separation larger than θ for the i th cluster in snapshot z_j with source plane z_k ; Ω is the solid angle of the survey under consideration, L^3 is simulation volume, and n_k is the number density of background galaxies in the bin about source plane z_k . The quantity V_j is the effective volume represented by the snapshot

$$V_j \equiv \int_{\frac{z_j+z_{j-1}}{2}}^{\frac{z_j+z_{j+1}}{2}} \frac{dV}{d\Omega dz}, \quad (8)$$

where $\frac{dV}{d\Omega dz}$ is the cosmological volume element. Hence, we take the clusters in the snapshot at redshift z_j to be representative of the lensing rate in the volume of the light cone over the redshift interval $[\frac{z_j+z_{j-1}}{2}, \frac{z_j+z_{j+1}}{2}]$.

Finally, in what follows we will often use the effective

cross section of a cluster, which we define as

$$\sigma_{\text{eff}}(> \theta) \equiv \frac{\sum_k n_k \bar{\sigma}_k(> \theta)}{\sum_k n_k}. \quad (9)$$

We defer a discussion of the counts of background galaxies in each source redshift bin, n_k , to § 7.1.

3.1. Adding Brightest Cluster Galaxies

Several groups have considered the degree to which cluster galaxies alter the cross section for producing giant arcs. Meneghetti et al. (2000) and Flores et al. (2000) studied the influence of cluster galaxies (besides the BCG), and found them to be generally unimportant. The effects of the central brightest cluster galaxy (BCG) were considered by Meneghetti, Bartelmann, & Moscardini (2003b), DHH, and Ho & White (2004). These studies found that BCGs increase the lensing cross section for arc separations small enough that the mass enclosed within the arc radii has a significant baryonic component. Specifically, DHH and Ho & White (2004) found that for arc radii $\gtrsim 10''$, the difference in the number of arcs for pure dark matter clusters versus clusters including BCGs was not dramatic.

In order to account for the effects of BCGs on the giant arc cross sections, we artificially add baryons to the centers of each cluster by ‘painting’ BCGs onto the dark matter surface density. Similar to the procedure in DHH, we model the mass profile with singular isothermal spheres (SIS), which accurately represent strong lensing by elliptical galaxies (see e.g. Kochanek et al. 2000). There it was found that the BCG enhancement of the cross section depended sensitively on the concentration of the central galaxy, parameterized by the velocity dispersion of the SIS; whereas varying the total mass of the central galaxy (i.e. the extent of the SIS) had a negligible effect. We thus choose to keep the mass of the central galaxy to be a fixed fraction $M_{\text{baryon}} = 0.003 M_{\text{FOF}}$ of the mass of the dark halo.

In the absence of a theory of BCG formation, we use a simple prescription for assigning velocity dispersions to the BCGs, scaling it with the mass of the dark matter halo. Edge & Stewart (1991) found a strong correlation between the optical luminosity of BCGs and the X-ray temperature of a large sample of galaxy clusters, with scaling $L_{\text{BCG}} \propto T_X^{8/10}$. Because BCGs lie on the fundamental plane of elliptical galaxies (Oegerle & Hoessel 1991), they obey the Faber & Jackson (1976) relation $L \propto \sigma^4$. Combining these scaling relations with the mass–temperature relation for X-ray clusters, $T_X \propto M^{2/3}$, gives $\sigma \propto M^{2/15}$. Normalizing this relationship to the Coma cluster gives

$$\left(\frac{\sigma}{300 \text{ km s}^{-1}} \right) = \left(\frac{M_{\text{FOF}}}{10^{15} h^{-1} M_\odot} \right)^{2/15}, \quad (10)$$

where we took the velocity dispersion of the BCG in Coma to be $\sigma = 323 \text{ km s}^{-1}$ (Fisher, Illingworth, & Franx 1995) and converted the X-ray temperature of Coma, $T_X = 8.0 \text{ keV}$ (Edge & Stewart 1991), to a FOF group mass ($b = 0.2$) using the prescription described in White (2001) (see also Hu & Kravtsov 2003).

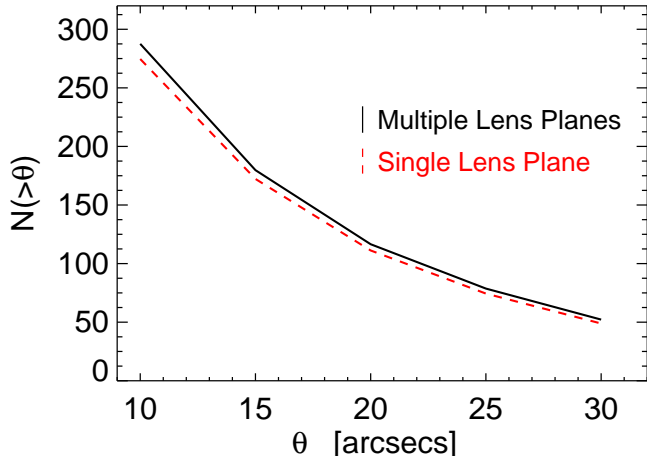


FIG. 2.— Cumulative distribution of giant arc separations for both single plane (dashed red) and multi plane (solid black) ray tracing simulations. Our full ray-tracing simulations show that line of sight projections have a modest effect, $\lesssim 7\%$, on the statistics of giant arcs with separations $\theta \gtrsim 10''$.

4. QUANTIFYING THE EFFECT OF MATTER IN THE LIGHT CONE

A question of recent interest has been the importance of projections of large-scale structure in the line of sight towards strong lenses. Wambsganss et al. (2004b) have suggested that projections of large scale structure significantly (~ 20 – 30%) increase strong lensing cross sections, using heuristic arguments. In this section, we quantify the effect of projections on giant arc cross sections using full ray tracing simulations.

We generalized our ray tracing code to compute lensing by matter at different redshifts using the multiple lens plane algorithm (see e.g. Schneider et al. 1992). This allows us to include the strong lensing effect of the large scale structure in the light cone between the source plane and the observer. This code was used in Dalal, Hennawi, & Bode (2005) to study the effect of projections of large scale structure on strong lensing cosmography, and a full description can be found there. Here, briefly summarize the essential features of the code.

We sliced through our $320 h^{-1}$ Mpc simulation cube to produce lens planes spaced every $160 h^{-1}$ Mpc with angular size roughly $20'$, so that the physical side length of the projected planes telescopes with increasing distance from the observer at $z = 0$. A total of 243 pairs of planes were produced for each of 19 redshifts between $z = 0 - 6.37$. The cosmic mean density was subtracted from each plane, and the lightcone was tiled by randomly selecting a pair of planes for each redshift, resulting in a total of 38 lens planes per realization. This procedure and the simulation outputs are identical to those used by Wambsganss et al. (2004a,b).

Ideally, we would compute arc cross sections simply by generating many such realizations and ray tracing over the entire $20'$ field. However, because the computation of reliable mean cross sections requires averaging over a large number of different cluster orientations, this approach would not be computationally feasible: we would spend the vast majority of our time ray tracing blank

regions of sky far from any clusters which would contain no giant arcs. To circumvent this practical constraint, we simply insert an extra lens plane containing the massive clusters for the lens redshift or snapshot that we consider. We ray trace only a $4 h^{-1}$ Mpc FOV around each cluster and project through the same number of different orientations as described in the previous section. However, each orientation now also includes a different random realization of the 38 lens planes to account for the large scale structure along the line of sight. This allows us to compute the total orientation-averaged strong lensing cross section for the clusters in this snapshot, but with the additional effect of large scale structure in the light cone. A direct comparison can then be made to the ray traces which included the clusters alone, as the orientation averaging is identical for both cases. We will refer to the ray traces which include large scale structure along the line of sight as the ‘Multi-Plane’ simulation and those which include only the clusters as the ‘Single-Plane’. An example of the critical curves of a massive cluster with and without the line of sight lens planes is shown in Figure 3 of Dalal, Hennawi, & Bode (2005). There it can be seen that the critical curves are only slightly affected by the line of sight density fluctuations. Note that in order to accurately compute the angular separations of the arcs from the cluster, we must take into account the deflection of the cluster center, which can be as large as $\sim 1'$, by lensing from the large scale structure between the observer and lens redshift.

We ray traced through a total of 13,594 unique projections of the 878 clusters in our simulation volume for the snapshot at $z_d = 0.41$. The source plane redshift was set to $z_s = 2.0$. BCGs were not added to the dark matter mass distribution for this analysis. In Figure 2 we compare the cumulative distribution of giant arc separations for the ‘Multi-Plane’ and ‘Single-Plane’ ray tracing simulations. It is clear that large scale structure projections do not have a significant effect on the abundance of giant arcs, as the largest difference between the two abundances is $\lesssim 7\%$. Wambsganss et al. (2004b) reported a larger effect, $\sim 25\%$, for a similar source redshift plane, based on qualitative arguments regarding the fraction of surface mass density pixels which became super-critical because of contributions from multiple lens planes. Their larger frequency of multi-plane lensing are most likely smaller separation, $\theta \lesssim 10''$, galaxy scale lensing events which would not be considered giant arcs. Our full ray-tracing simulations show quantitatively that line of sight projections have a modest effect on the statistics of giant arcs with separations $\theta \gtrsim 10''$.

5. ANALOG HALOS

To elucidate which properties of CDM halos are most important for strong lensing, we have measured structural properties for our simulated clusters and generated synthetic analog halos which preserve one or more of these properties. By comparing the lensing strengths of the synthetic analog halos to the N-body halos, we are able to quantify the significance of various aspects of halo structure for strong lensing.

The key structural characteristics we measure for our halos are the radial density profile $\rho(r)$ measured with respect to the most bound particle, the inertia tensor of the particle distribution, and the degree of substructure.

We have generated four types of analog halos:

1. **Spherical** analogs preserve the radial density profile $\rho(r)$ but are spherically symmetric.
2. **Triaxial** analogs are similar to spherical analogs, however they preserve the inertia tensor of the cluster core.
3. **Clumpy core** analogs are similar to triaxial analogs, however the particle distribution within the cluster core is left unchanged while the mass exterior to the core is smoothed triaxially.
4. **No substructure** analogs preserve the particle distribution, except for particles within massive subhalos, which are triaxially redistributed.

For the simplest cases of spherical and triaxial analogs which we describe below, these halos mirror the types of simplified analytical models which have been used to describe strong lensing by galaxy clusters previously in the literature (Bartelmann 1996; Meneghetti, Bartelmann, & Moscardini 2003a; Oguri et al. 2003; Oguri & Keeton 2004). It is well known that these simple models underpredict the number of giant arcs (Meneghetti, Bartelmann, & Moscardini 2003a). Our analog halos have the added advantage that they exactly reproduce the joint distribution of halo shapes and concentrations in the simulation volume. Thus, they represent the case of the more sophisticated analytical models which attempt to account for the joint distributions of halo shapes and concentration measured from numerical simulations (Jing & Suto 2002; Oguri et al. 2003; Oguri & Keeton 2004). Although analytical models for the distribution of substructure in dark matter halos exist (e.g. Sheth 2003; Sheth & Jain 2003; Oguri & Lee 2004), computing strong lensing cross sections for such models is sufficiently cumbersome that it has not yet been undertaken. Our ray tracing computation for the no-substructure halos allow us to quantify the effect of dense substructure on the efficiency for producing giant arcs. Because the clumpy core analog halos are roughly identical to their parents inside of an average overdensity of $\sim 10,000$, but are smooth ellipsoids outside of this contour, a comparison with their parent halos can quantify the degree to which the structure of the large scale mass distribution changes strong lensing cross sections. We note that some of these issues have already been explored in Meneghetti, Bartelmann, & Moscardini (2003a). There the differences between elliptical (triaxial) and real dark matter halos was quantified via a multipole analysis in Fourier space. Our method of Analog Halos is complementary, and because we modify these halos in real space, we can pinpoint the particular halo properties which are important to strong lensing.

5.1. Generating Analog Halos

Spherical analog halos are generated by randomly redistributing the angular coordinates of particles while holding fixed their radial coordinates. The radial profile $\rho(r)$ of each spherical analog is thus identical to its parent halo. Note that all radii are measured with respect to the most bound particle in the cluster.

To generate triaxial analog halos we follow a similar procedure as for the spherical case. For each particle we compute the ellipsoidal radius (see e.g. Jing & Suto 2002)

$$R_e = \sqrt{\frac{X^2}{A^2} + \frac{Y^2}{B^2} + \frac{Z^2}{C^2}}, \quad (11)$$

as well as $A = (q_2 q_3)^{-1/3}$, $B = q_2 A$, and $C = q_3 A$, where the coordinates X, Y, Z are measured along the principal axes of the core (i.e. the eigenvectors of the inertia tensor \mathbf{Q} , see eqn. 6). Each particle is then randomly mapped onto the surface of the ellipsoid defined by constant R_e . This procedure preserves the density profile in ellipsoidal coordinates $\rho(R_e)$ (Jing & Suto 2002) and also maintains the axis ratios and principal axes of the core of the original N-body halo.

The no-substructure analog halos are generated by redistributing all of the particles linked into FOF subhalos ($b = 0.05$) with masses $M_{\text{FOF}} > 10^{11.5} h^{-1} M_\odot$, except for those in the largest subhalo, which are left untouched. The subhalo particles are redistributed along the ellipsoid defined by R_e in eqn. (11) using the principal axis directions and axis ratios of the core—i.e. using exactly the same procedure as for the triaxial analog halos—thus also preserving $\rho(R_e)$. As discussed in §2.3, the FOF algorithm with linking length $b = 0.05$ links particles into groups enclosed by an average overdensity of $\sim 10,000$. These analog halos are thus identical to their corresponding N-body halos except that all substructures containing $M > 10^{11.5} h^{-1} M_\odot$ within a mean overdensity of 10,000 have been smoothed out.

We generate the clumpy core analog halos in exactly the same way as the triaxial case except that the particles in the most massive subhalo identified by the FOF with $b = 0.05$, i.e. the cluster core, are left untouched. Thus the Clumpy Core analog halos are roughly identical to their parents inside of a mean overdensity of $\sim 10,000$, but smooth and nearly identical to the ‘Triaxial’ analog halos outside of this overdensity.

Figure 3 compares the cluster lens in our simulation with the largest lensing cross section to all of its different analog halos. This cluster, taken from a snapshot at $z_d = 0.41$, has mass $M_{\text{vir}} = 8.1 \times 10^{14} h^{-1} M_\odot$ and concentration $c_{\text{NFW}} = 6.9$. The axis ratios of the core are $q_2 = 0.46$ and $q_3 = 0.40$. In Figure 4, we compare the radial density profile of this cluster to the profiles of the different analog halos. The spherical case is not shown because its radial density profile is identical to the parent by construction. Note that although we keep the ellipsoidal radius R_e fixed when redistributing particles to create the triaxial, no substructure, and clumpy core analog halos, in practice the radial profiles $\rho(r)$ are nevertheless preserved to a high degree of accuracy.

5.2. Lensing Comparison

We generated each type of analog halo for all 878 clusters in the the snapshot at $z_d = 0.41$. We ray traced through every cluster for a source plane at $z_s = 2.0$, averaging over the same orientations for each halo (see § 3), and computed the cumulative distribution of image splittings following eqn. (7). Since our aim is to understand which characteristics of the dark matter distribution are most important for strong lensing, BCGs were not added to the mass distribution for this analysis. In Figure 5 we

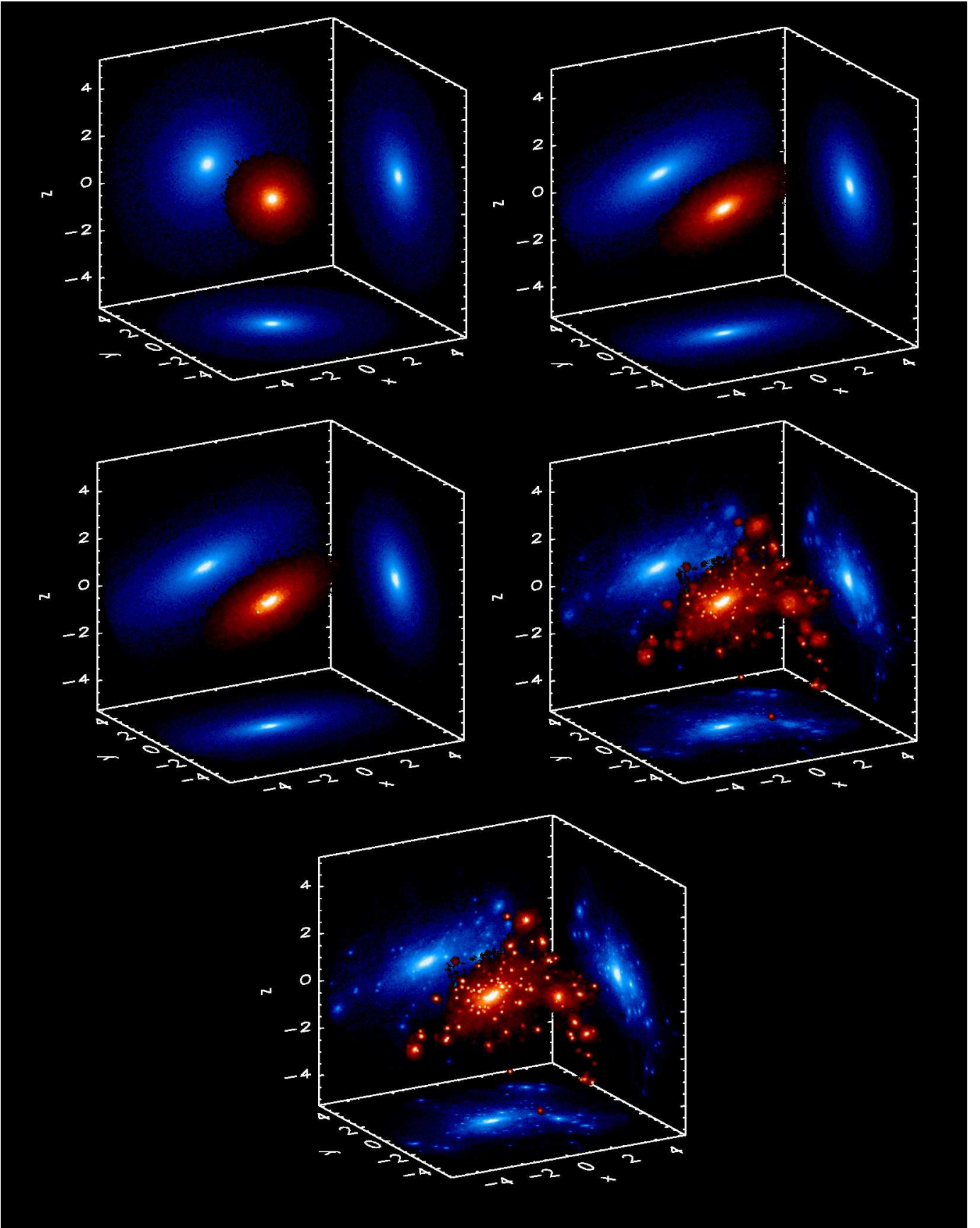


FIG. 3.— Density distributions of four different types of analog halos compared to the original parent. The surface density for three projections are shown on the coordinate axis planes to aid visualization. The spatial axes are in units of comoving h^{-1} Mpc and both density (2-d and 3-d) colormaps are logarithmically stretched. Upper left is the spherical analog, the upper right is the triaxial analog, middle left is the clumpy core analog, middle right is the no substructure analog, and the parent halo is depicted at the bottom. The radial mass profiles of the analog halos are compared to that of the parent halo in Figure 4.

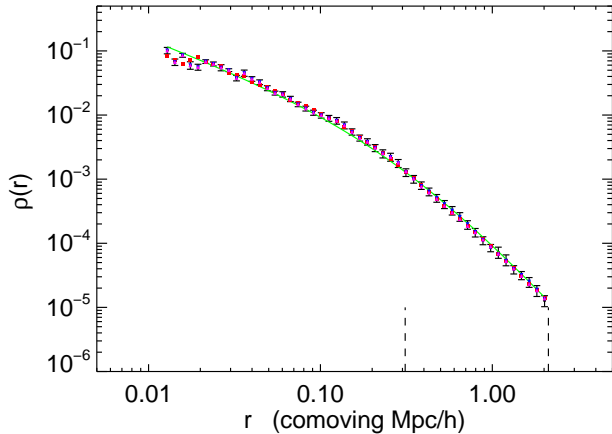


FIG. 4.— Comparison of radial density profile $\rho(r)$ of analog halos shown in Figure 3 to original parent halo. The y-axis has units of $h^{-1} \text{ M}_\odot/\text{pc}^3$. The black points and error bars are the density profile and bootstrapped variances of the original parent halo. The solid green line is the best fit NFW profile. The inner and outer dashed vertical lines indicate the locations of the scale radius and virial radius for the best fit NFW profile, respectively. Red squares, magenta triangles, and blue upside down triangles, show the density profile of triaxial, and clumpy core analog halos, respectively. The spherical case is not shown because its radial density profile is identical to the parent halo by construction. Although we kept the ellipsoidal radius R_e fixed when redistributing particles for the analog halos shown, the radial profiles are nevertheless preserved to a high degree of accuracy.

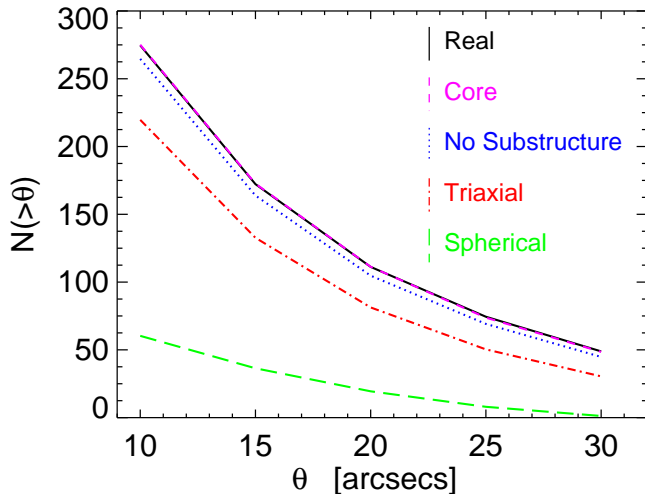


FIG. 5.— Comparison of the number of giant arcs on the entire sky for original and analog halos. The black curve is the cumulative distributions of giant arcs lensed by the original ‘parent’ in the snapshot at redshift $z_d = 0.41$. The source plane was at $z_s = 2.0$, and the density of background galaxies in the redshift range $[1.75, 2.5]$ was computed according to the discussion in § 7.1. The green (long dashed) curve is the distribution of arc separations if all clusters in the simulation volume are replaced by their spherical analog halos. The red (dot-dashed), blue (dotted) and magenta (short dashed) curves show the same quantity but for triaxial, no substructure, and clumpy core analog halos, respectively. The data plotted above are also shown in Table 1.

compare the number of giant arcs produced by the real and analog halos, assuming an area equal to the entire

sky. The data used to construct this figure is given in Table 1.

From the data in the table, we see that spherical halos underpredict the abundance of giant arcs by a factor as large as 50 and triaxial models fall short by a factor as much as 60%. These results are consistent with the findings of Meneghetti, Bartelmann, & Moscardini (2003a). Because the distribution of halo concentrations and shapes of the parent halos is exactly reproduced in our analog halos, we conclude that even the more complicated analytical models which convolve analytical cross sections with the distributions of halo concentrations and shapes (Oguri et al. 2003; Oguri & Keeton 2004), will underpredict the number of cluster lenses by a large amount. It is noteworthy that triaxiality increases the number of giant arcs by a factor of 4-25 compared to the spherically symmetric halos. This is because the shallow density cusps $\rho \propto r^{-1}$ of CDM halos result in an extreme sensitivity to triaxiality, as has been emphasized by several authors (DHH; Dalal & Keeton 2003; Bartelmann & Meneghetti 2004).

From a comparison of the real halos to the no substructure analogs, it is apparent that projections of dense substructure onto the small radii probed by strong lensing has a relatively modest effect on the lensing cross sections, increasing the total number of arcs by $\sim 5-10\%$. Meneghetti et al. (2000) came to similar conclusions about changes in lensing cross sections caused by baryonic substructure (cluster galaxies) which have small masses $\lesssim 10^{12} h^{-1} \text{ M}_\odot$. Here we find a similar result for dark matter substructure, which can be much more massive for the extreme case of a binary or merging cluster. We revisit the effect of substructure on strong lensing in § 6, when we statistically quantify the properties of cluster lenses.

Recall that the clumpy core analog halos are identical to the original parent halos inside a mean overdensity of 10,000, but are smooth ellipsoids outside of this contour. The close agreement between the clumpy core analogs and the parent halos, indicates that halo substructure and the large scale mass distribution do not significantly influence strong lensing cross sections. The number of giant arcs produced by CDM halos is *primarily determined by the mass distribution within a mean overdensity of $\sim 10,000$.*

The difference between the cross sections for triaxial halos and the full N-body halos indicates that some systematic departure from ellipsoidal symmetry, on average, enhances lensing strength. Some possibilities for this include substructure on very small scales, or perhaps lopsidedness in the form of boxiness or diskiness in the isodensity contours. Naively, we would not expect massive substructures to persist in the high-density cores of clusters since the dynamical friction timescale is much shorter than the Hubble time. We have attempted to detect whether larger-scale departures from ellipsoidal symmetry enhance lensing cross section by running a principal component analysis on the halo density profiles. The results of this analysis were unclear: the principal components we recovered with high signal to noise appeared to correspond to varying concentration and ellipticity, with no other significant components apparent. This point warrants future study, since it suggests that the abundance of giant arcs is sensitive to the detailed

TABLE 1
ANALOG HALO COMPARISON

Type	$N(\theta > 10'')$	$N(\theta > 15'')$	$N(\theta > 20'')$	$N(\theta > 25'')$	$N(\theta > 30'')$
Real	274.6	172.3	111.2	74.4	48.9
Clumpy Core	275.1	172.6	111.3	73.8	48.5
No Substructure	264.7	163.9	104.7	69.1	44.8
Triaxial	219.7	132.7	81.3	50.3	30.4
Spherical	60.3	36.4	19.4	8.0	1.2

NOTES— Comparison of the number of giant arcs produced by real halos to the number produced by analog halos. The quantity $N(\theta > 10'')$ is the cumulative number of of giant arcs on the entire sky for a source plane at $z_s = 2.0$. The data in this table are plotted in Figure 5.

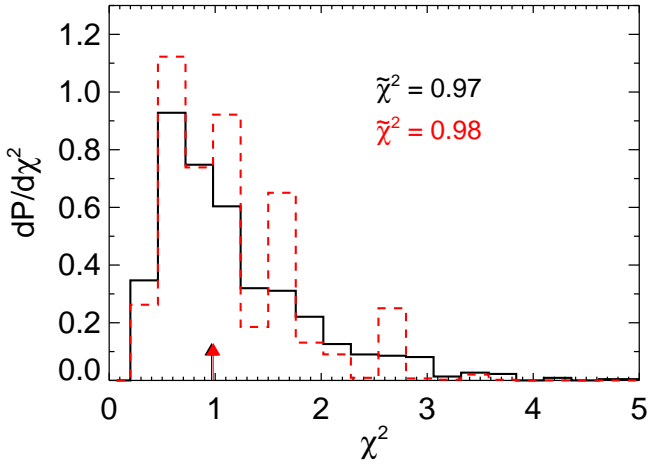


FIG. 6.— Lensing (dashed) and total (solid) distributions of the reduced χ^2 of the NFW fit to the number profile of each halo. The median of both the lensing and total distributions, indicated by the arrows, are labeled in the upper right. The fact that the median value of the total distribution is near unity gives us confidence that the NFW profile is providing a good fit to the simulated clusters and the bootstrapped σ_i are accurately describing the errors (see § 2.2). The similarity between the lensing and total distribution indicates that NFW profiles provide just as good a fit to lensing clusters as they do to the total population.

morphology of dark matter halos on small scales.

6. CHARACTERIZING THE CLUSTER LENS POPULATION

In this section we address the following question: How different is the population of lensing selected clusters from the general cluster population? Because cluster strong lensing is sensitive to the mass distribution interior to the NFW scale radius $r \lesssim 300 h^{-1}$ kpc, it provides a means to measure the concentration of clusters, especially when combined with larger scale mass measurements like weak lensing (Kneib et al. 2003; Gavazzi et al. 2003; Broadhurst et al. 2005b). It is thus interesting to quantify the degree to which these concentrations will be systematically higher than the typical cluster in the Universe. Besides concentration, other biases might exist. Are lensing clusters significantly more or less triaxial? Do they have more/less substructure? How likely is the major axis of a lensing cluster to be aligned with the line of sight?

We are in a position to answer these statistical questions because of the large number of clusters and ori-

entations that we have ray traced. Specifically, for the snapshot at $z_d = 0.41$ we ray traced through a total of 13,594 unique projections of the 878 clusters in our $V = (320 h^{-1} \text{ Mpc})^3$ simulation volume. This constitutes an increase of two orders of magnitude in both the number of clusters and number of orientations of any previous study. For the remainder of this section, we focus our statistical analysis on the clusters in this snapshot at $z_d = 0.41$. Note that BCGs were added to the mass distributions of these clusters as described in § 3.1 and thus are included in the strong lensing cross sections. However, we measured the cluster parameters (mass, concentration, triaxiality) from the dark matter particle distributions alone.

We define the probability distribution of the cluster parameter u (such as mass, concentration, axis ratio, etc.)

$$P_{\text{lens}}(u) = \frac{1}{\sum \sigma_{\text{eff}}} \frac{d\sigma_{\text{eff}}}{du}, \quad (12)$$

where $\sum \sigma_{\text{eff}}$ is the total effective cross section of all the clusters (see eqn. 9) in our simulation volume and $\frac{d\sigma_{\text{eff}}}{du}$ is the differential distribution of the statistic u , which we compute by summing the total cross section with u between u and $u + \Delta u$. In what follows, we use $\sigma_{\text{eff}}(\theta > 15'')$, the effective cross section for forming giant arcs with separations $> 15''$. A comparison of the lensing distribution $P_{\text{lens}}(u)$, to the probability distribution of the total cluster population $P_{\text{tot}}(u)$ will indicate the degree to which the lenses constitute a biased sample.

In what follows we will compare the NFW parameters of cluster lenses to the total cluster population. This comparison is clearly only sensible provided that NFW profiles provide a good fit to the cluster lenses. In Figure 6 we compare the distribution of the reduced χ^2 of the NFW profile fits (see eqn. 3) for the cluster lenses to the those for the total population. The similarity of the distributions indicates that NFW profiles provide just as good a fit to lensing clusters as they do to the total population. Furthermore, the fact the reduced $\chi^2 \sim 1$ indicates that NFW profiles provide good fits to the mass distributions of our clusters.

6.1. Mass and Concentration

In the left panel of Figure 7 we show a scatter plot of the orientation-averaged effective cross sections $\sigma_{\text{eff}}(\theta > 15'')$ against virial mass, for all 878 of the clusters in the snapshot at $z_d = 0.41$. The colors and sizes of the points indicate the value of the concentration of each cluster. The histogram shows the strong lensing probability av-

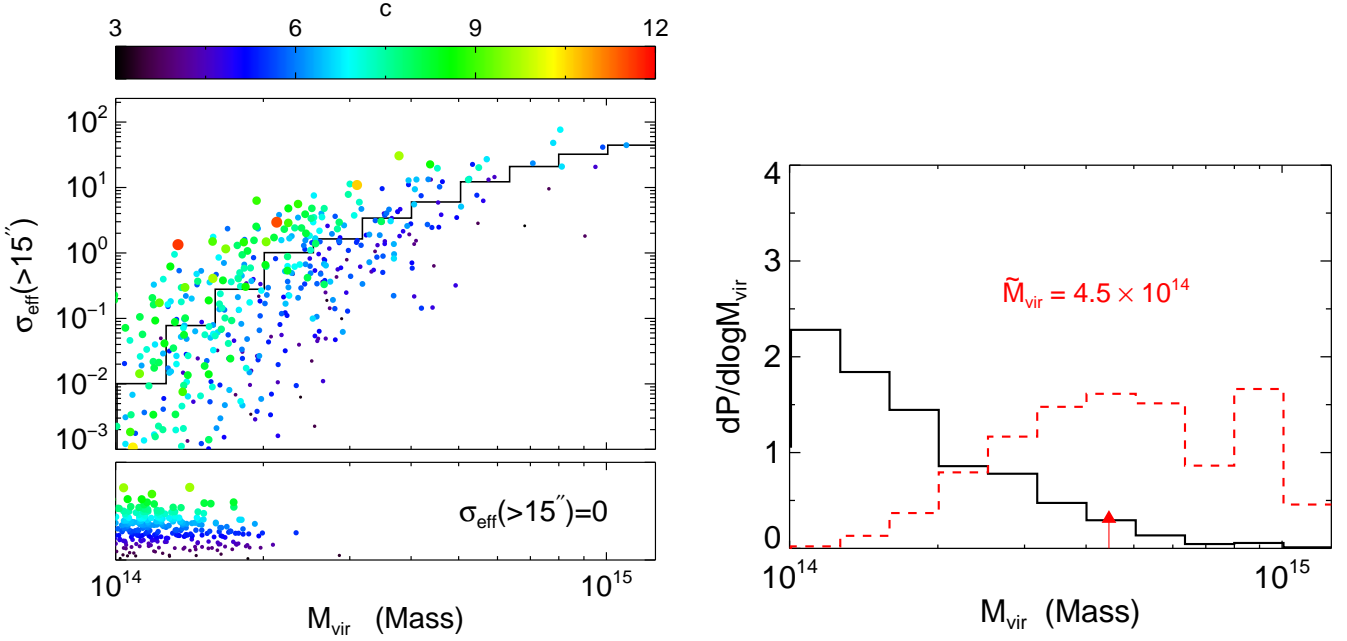


FIG. 7.— *Left*: Scatter plot of effective strong lensing cross section for forming giant arcs with $\theta > 15''$ against cluster mass, for clusters at $z_d = 0.41$. Each point corresponds to a cluster in our simulation volume and the cross sections have been averaged over all orientations (see § 3). The y-axis has units of arcsec^2 , and the colors and sizes of the points indicate the value of the lens strength parameters κ_s (see § 2.2). For $M \gtrsim 10^{15} h^{-1} M_\odot$, all clusters are effective strong lenses; whereas at lower masses $M \lesssim 3 \times 10^{14} h^{-1} M_\odot$ only the most concentrated members of the population can multiply image quasars. The histogram shows the mean strong lensing probability averaged over mass bins of width 0.1 in $\log_{10} M$. Clusters which have zero strong lensing cross section for all orientations are plotted in the lower panel, where we have stretched the y-axis so that the points do not all overlap. *Right*: Comparison of the probability distribution of the virial mass, $P_{\text{ens}}(\log_{10} M_{\text{vir}})$ of cluster lenses (dashed red curve) to the mass function, normalized to unity over the mass range considered. (solid black curve). These are the same clusters at $z_d = 0.41$ shown in the left panel. The bin spacing is the same as in the left panel. The red histogram $P_{\text{ens}}(\log_{10} M)$ can be obtained from the scatter plot in the left panel by summing the values of the cross sections in each mass bin and dividing by the total cross section integrated over all bins (see eqn. 12). The mean value of $\log_{10} M$ of the cluster lens sample is $M_{\text{vir}} = 10^{(\log_{10} M)_{\text{lens}}} = 4.5 \times 10^{14} h^{-1} M_\odot$, indicated by the arrow.

eraged over mass bins of width $d\log_{10} M = 0.1$. Subcritical clusters which had zero effective cross sections are plotted in the lower panel, where we have arbitrarily stretched the vertical axes so the points do not overlap. The scatter plot illustrates the range of cross sections which exist in a given mass bin. In addition, it shows that for the largest masses characteristic of superclusters, $M \sim 10^{15} h^{-1} M_\odot$, all clusters are effective strong lenses, whereas at lower masses $M \lesssim 3 \times 10^{14} h^{-1} M_\odot$, only the more concentrated members of the population are strong lenses. Notice the extremely steep dependence of the lensing cross section on mass: the mean cross section changes by nearly four orders of magnitude over a single decade in mass. In the right panel, we compare the probability distribution $P_{\text{ens}}(\log_{10} M)$ (dashed red curve) to the cluster mass function normalized to unity over the mass range $M > 10^{14} h^{-1} M_\odot$ considered (solid black curve). The bin spacing in the right panel is the same as in the left panel. The red histogram $P_{\text{ens}}(\log_{10} M)$ can be obtained from the scatter plot in the left panel by summing the values of the points in each mass bin and normalizing the histogram by the total number of lenses (see eqn. 12). The median value of $\log_{10} M$ for the cluster lens sample is $M = 10^{\log_{10} \tilde{M}_{\text{lens}}} = 4.5 \times 10^{14} h^{-1} M_\odot$.

The left panel of Figure 7 suggests that lensing selected cluster samples are likely to show significant concentration bias. Since we have seen that cross section is such a steep function of cluster mass, it is desirable to first normalize out the mass dependence of cluster concen-

tration. Thus we consider the distribution of the ratio $c_{\text{vir}}/c_{\text{vir}}(M)$, where $c_{\text{vir}}(M)$ is some kind of average concentration. Because simply computing the mean concentration in mass bins will be sensitive to outliers and very noisy at the high mass end where we have few clusters, we must be careful about the fitting procedure. In Figure 8 we show a scatter plot of concentration versus virial mass measured from the clusters in our simulation volume at $z_d = 0.41$. The blue curve is a second order B-spline fit to points with breakpoints set every 175 clusters ordered by mass. This fit was computed iteratively with 3σ outliers rejected at each iteration until convergence was achieved. Bullock et al. (2001) measured the trend $c = \frac{9}{(1+z)}(M/M_*)^{-0.13}$ from a large ensemble of numerically simulated clusters, where M_* is the nonlinear mass at $z = 0$ which is $M_* = 1.3 \times 10^{13} h^{-1} M_\odot$ for our cosmology. The red dashed curve in Figure 8 curve shows the result of adopting the Bullock et al. (2001) power law scaling and fitting the median concentration in five logarithmically spaced mass bins for the linear amplitude. We get $c = \frac{12.3}{(1+z)}(M/M_*)^{-0.13}$, i.e. our average concentrations are 37% higher than Bullock et al. (2001)⁷. Our

⁷ This disagreement is likely due to differences in the halo fitting procedure and also possibly because of the different cosmological model simulated. Bullock et al. (2001) truncate halo radii when halos overlap and they only fit particles *bound* to the halo. We argued in § 2.2 that neither practice is appropriate to the context of gravitational lensing.

B-spline fit is in near agreement with the relation found by Bullock et al. (2001), although the mass scaling is not quite as steep.

The lensing and total distributions of $c/c(M)$ are shown in the right panel of Figure 8. The median of the total distribution is consistent with unity to better than 1%, indicating that the average concentration shown in the left panel of Figure 8 is a good fit to $c(M)$. We see that the cluster lens population has three dimensional concentrations $\sim 18\%$ higher than the average cluster at a similar mass.

6.2. Triaxiality and Orientation Bias

In this section we investigate alignment bias and study the effect of triaxiality on strong lensing probability. The lensing and total distributions of the absolute value of the cosine of the angle between the line of sight and the major axis direction of the cluster, $|\cos\theta| = \hat{\mathbf{z}} \cdot \hat{\mathbf{V}}_a$, are shown in the left panel of Figure 9. The thin (black) line is the distribution for all clusters, which is flat as expected. The axis ratio q_2 is divided into three groups with equal total lensing probability. The magenta (dotted), blue (dashed), and green (dot-dashed) curves are individual lensing contributions from clusters with axis ratio q_2 in the lower third $q_2 < 0.50$ (most triaxial), middle third $0.50 < q_2 < 0.66$, and upper third $q_2 > 0.66$ (least triaxial). These contributions sum to give the total lensing distribution, which is the thick red (solid) curve. The median value for the lensing clusters is $|\cos\theta|_{\text{lens}} = 0.67$, indicating significant alignment bias. Furthermore, the alignment bias is larger for the more triaxial clusters, as expected. Our findings disagree with the discussion in Bartelmann, Steinmetz, & Weiss (1995) who also compared the orientation of the cluster principal axes to the line of sight and found no significant correlation between the two. Because this study only ray traced 3 different projections through 13 clusters, it is likely that they did not have the statistics to measure the correlation which we detect with high significance.

Despite this large tendency for lensing clusters to be aligned with the line of sight, the lensing population has nearly the same distribution of axis ratios as the total cluster population. This is the clear indication of Figure 10, which shows the distributions of the axis ratios q_2 and q_3 (shown in the left and right panels, respectively). The lensing distributions are nearly indistinguishable from the total cluster population.

We have detected significant alignment bias between the line of sight and the principal axis direction of the clusters, and furthermore we argued in §5 that triaxiality significantly increased the total lensing cross section for CDM clusters. On the other hand, Figure 10 indicates that lensing clusters have the same distribution of axis ratios as the total cluster population. These two statements seem to contradict each other. If triaxiality enhances lensing cross sections and if there is a tendency for strong lenses to be aligned with the line of sight, why are lensing clusters not systematically more triaxial than the total population?

One possible explanation for this apparent contradiction is that the shape of a dark halo is correlated with its concentration, as might be expected on dynamical grounds. Allgood et al. (2005) have found that simulated dark halos which have recently collapsed are more

triaxial (q_2 smaller) and less concentrated, whereas halos which have collapsed in the more distant past are on average less triaxial (q_2 larger) and more concentrated. Dynamically old clusters formed when the Universe was more dense and hence are more concentrated, and similarly have had more time to relax and hence should be less triaxial. Indeed, a similar trend exists in our sample of clusters as is shown in the scatter plot of normalized concentration versus axis ratio in Figure 11.

6.3. 2-D vs. 3-D concentration

Because strong lensing probes the mass in projection, the three dimensional concentration considered above is not an observable. Rather, the two-dimensional concentration is measured from detailed modeling of the arcs and image positions. For a given 3-D concentration, we expect an additional bias to exist in the distribution of 2-D concentrations since lensing clusters are triaxial and, as discussed above, tend to be viewed down their major axes. The left panel of Figure 12 indicates that this is indeed the case. There we show the lensing and total distributions of c_{2D}/c_{3D} , which is the two-dimensional concentration (for a given projection) normalized by the three-dimensional concentration of each cluster. The histogram is computed using the cross section for each of the 13,594 unique projections of the 878 clusters in our simulation volume. Note that median value of the total distribution deviates from unity by 6%. This bias relative to the three dimensional concentrations is caused by the fact that our two dimensional NFW profile fits underestimate the concentrations because we fit to the projection of a profile which extends to infinity (see discussion in § 2.2). Nevertheless, we see that the lensing distribution of c_{2D}/c_{3D} is biased by $\sim 19\%$ relative to the total distribution.

We compare the lensing and total distributions of the two dimensional concentrations in the right panel of Figure 12. The concentrations of lensing clusters are 34% larger than those of the total cluster population. This bias is caused by the combination of two effects. First, strong lensing clusters have three dimensional concentrations which are on average 18% larger than the typical cluster at the same mass, as is indicated by Figure 8. Second, given a three dimensional concentration, Figure 12 indicates that strong lensing prefers the projections through clusters which give $\sim 19\%$ higher concentrations. This 34% concentration bias should be kept in mind when comparisons are made between concentrations measured from modeling observed strong lenses to the mean concentrations measured from N-body simulations.

The foregoing discussion has bearing on the recent measurements of anomalously high concentrations from detailed modeling of individual lensing clusters. From combined weak and strong lensing analyses, Kneib et al. (2003) measured a best fit concentration of $c_{\text{NFW}} = 22$ for CL0024+1654, while Gavazzi et al. (2003) measured $c_{\text{NFW}} = 12$ for MS 2137.3–2353 (but see Dalal & Keeton 2003), and Broadhurst et al. (2005b) measured $c_{\text{vir}} = 13.7$ for Abell 1689. It is unlikely that the brightest cluster galaxies in these clusters increase the concentrations over our expectation for dark matter alone.⁸ Note that

⁸ For CL0024+1654 and Abell 1689 the arcs occur at large radii

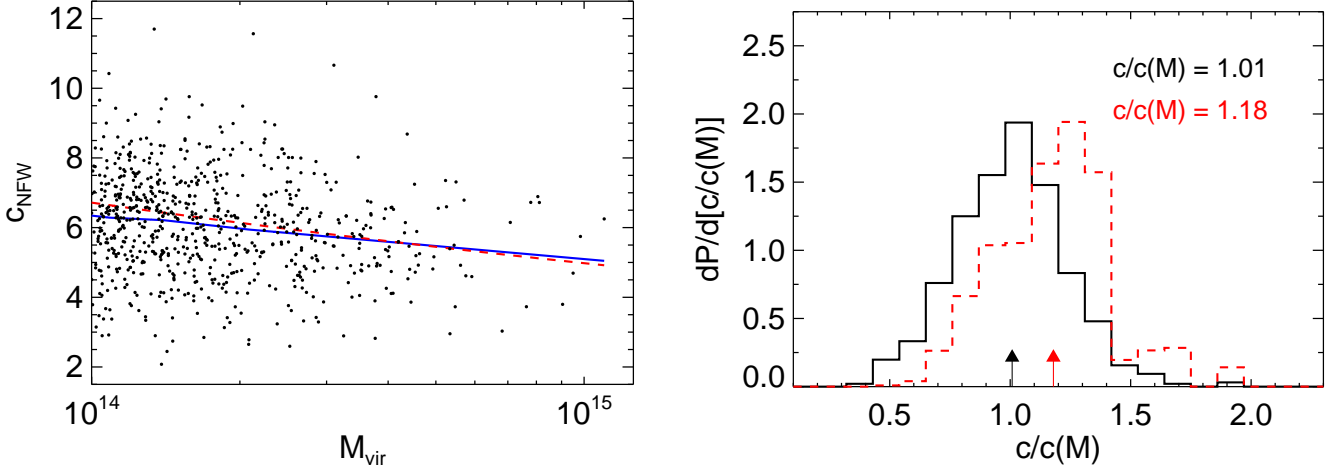


FIG. 8.— *Left:* Scatter plot of cluster concentration versus virial mass for all the clusters in our simulation volume at $z_d = 0.41$. The solid blue curve is a second order B-spline fit to the points with breakpoints set every 175 clusters ordered by mass. To reduce sensitivity to outliers, this fit was computed iteratively with 3σ outliers rejected at each iteration until convergence was achieved. The dashed red curve shows the fit, $c_{\text{vir}} = \frac{12.3}{(1+z)} (M/M_*)^{-0.13}$, which is the result of adopting the Bullock et al. (2001) power law scaling and fitting the median concentration in five logarithmically spaced mass bins for the amplitude. The B-spline fit (solid blue line) is in near agreement with the relation found by Bullock et al. (2001), although the mass scaling is not quite as steep. *Right:* Lensing (dashed) and total (solid) distributions of the ratio $c/c(M)$. Arrows indicate the median of the distributions. The fact that the median of the total population is consistent with unity indicates that our fit for $c(M)$ has effectively removed the average mass scaling from the concentration. Cluster lens have three dimensional concentrations 18% higher than the typical cluster with similar mass.

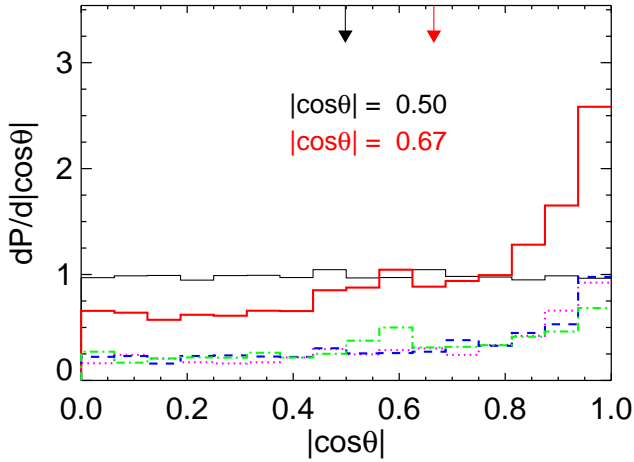


FIG. 9.— The lensing and total distributions of the absolute value of the cosine of the angle between the line of sight and the major axis direction of the cluster. The thin (black) line is the intrinsic distribution, which is flat as expected. The axis ratio q_2 is divided into three groups with equal lensing probabilities. The magenta (dotted), blue (dashed), and green (dot-dashed) curves are individual contributions from clusters with axis ratio q_2 in the lower third $q_2 < 0.50$ (most triaxial), middle third $0.50 < q_2 < 0.66$, and upper third $q_2 > 0.66$ (least triaxial). These contributions sum to give the total distribution which is the thick solid (red) curve. The median of both the lensing and total distributions, indicated by the arrows, are labeled on the plot. The median for the lensing clusters is $|\cos \theta| = 0.67$, indicating significant alignment bias.

$\gtrsim 30''$, where the baryonic component contributes only a small fraction $\lesssim 10\%$ of the total mass enclosed by the critical curves (see e.g. Broadhurst et al. 2005a). Baryons are a larger concern for MS 2137.3–2353 because its arcs are at smaller radii $\lesssim 15''$, however Gavazzi et al. (2003) found that including a mass compo-

Kneib et al. (2003) and Gavazzi et al. (2003) use a convention for the NFW concentration, $c_{\text{NFW}} = r_{200}/r_s$, where r_{200} is the radius at which the average density is 200 times the *critical* density, which differs from our definition of $c_{\text{vir}} = r_{\text{vir}}/r_s$, where r_{vir} is the radius where the average density is $\Delta_{\text{vir}}(z)$ times the *mean* density. Converting these concentrations to our convention (White 2001; Hu & Kravtsov 2003), gives $c_{\text{vir}} = 26.2$ and $c_{\text{vir}} = 14.6$, for CL0024+1654 and MS 2137.3–2353, respectively.

These high concentrations are very puzzling, considering that the distribution in the right panel of Figure 12 predicts that the probability for $c_{2D} > 14$ is less than 2%. Why should the three best studied lensing clusters in the Universe all have concentrations on the tail of the concentration distribution? One possible explanation is that these clusters have been studied intensively because they are known to contain multiple giant arcs, and one might expect clusters with multiple high-surface brightness arcs to be even more biased than the general population of cluster lenses. While not implausible, Ho & White (2004) found that $\sim 40 - 50\%$ of massive clusters that produce giant arcs show multiple arcs, which suggests that multi-arc clusters are relatively common. A definitive solution to this puzzle of high observed concentrations will clearly require a large, homogeneously selected statistical sample of strong lensing clusters.

6.4. Substructure

In § 2.3, we defined three simple statistics which quantify the amount of substructure in a cluster. The first,

nent associated with the central galaxy did not significantly change the resulting concentration.

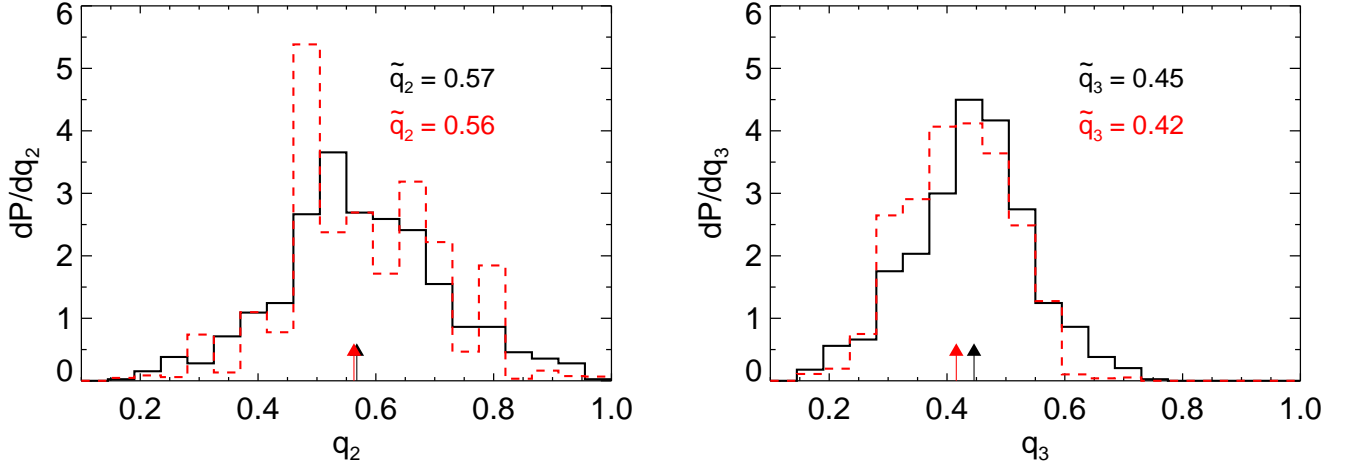


FIG. 10.— Lensing (dashed) and total (solid) distributions of the axis ratios. The left panel shows the distributions of the axis ratio q_2 and the right panel shows the distributions of q_3 . The mean of both the lensing and total distributions, indicated by the arrows, are labeled in the upper right corner of each plot. The lensing population has nearly the same distribution of axis ratios as the total cluster population.

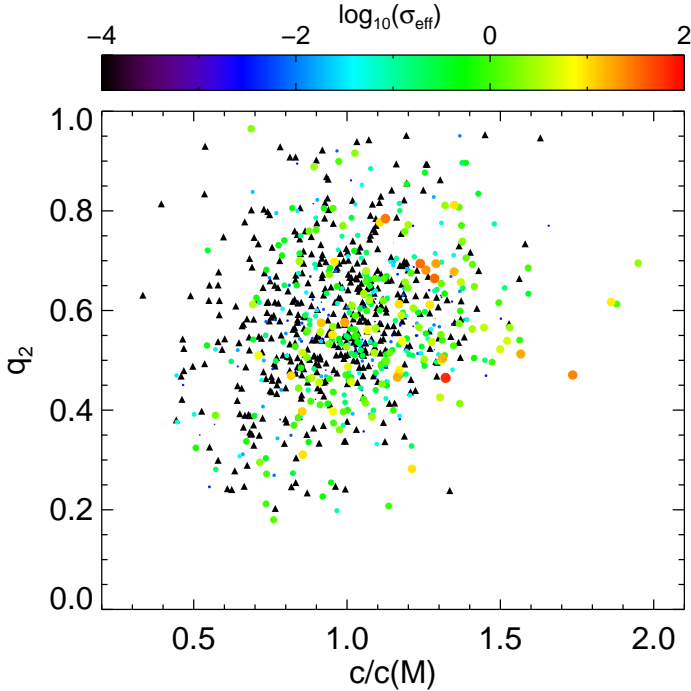


FIG. 11.— Scatter plot of normalized concentration, $c/c(M)$ versus axis ratio q_2 for the clusters in our simulation at $z_d = 0.41$. The black triangles show clusters with zero strong lensing cross section $\sigma_{\text{eff}} (> 15'')$ and circles show clusters with nonzero cross sections, where the colors and sizes of the points indicate the size of the cross section in units of arcsec^2 . Cluster with a large degree of triaxiality (small q_2) tend to be under concentrated; whereas, clusters which are less triaxial (large q_2) tend to be over concentrated. This correlation between q_2 and normalized concentration is expected on dynamical grounds (see discussion in § 6).

$M_{\text{sub-core}}$, is the ratio of the mass in substructures to the core mass of the cluster; the second, $M_{\text{sub-vir}}$, is the ratio of the mass in substructure to the virial mass of the cluster; and the third, $M_{2-\text{vir}}$, is the ratio of the most

massive substructure (i.e. second to the the cluster core) to the virial mass. The lensing and total distributions of these three statistics are shown in Figure 13.

A comparison of the lensing and total distributions of these statistics indicates that any correlation between strong lensing cross section and the presence of substructure is marginal at best. First, focusing attention on Figure 13, which is for substructures within the virial radius, the median of the statistic $M_{\text{sub-core}}$ for the lensing and total distributions suggests that lensing clusters have $\sim 10\%$ less substructure than the total cluster population. The mass in substructure normalized by the virial mass, $M_{\text{sub-vir}}$, is biased in the opposite direction by $\sim 10\%$ compared to the total cluster population. Both of these statistics consider all substructures $> 10^{12} h^{-1} M_\odot$ (see eqn. 5) and effectively integrate over the subhalo mass function. In contrast, the statistic $M_{\text{sub-2}}$ quantifies the binarity of the cluster and is expected to be largest for a cluster undergoing a major merger. The median value of $M_{\text{sub-2}}$ for lensing selected clusters is indistinguishable from the total cluster population.

The fact that $M_{\text{sub-2}}$ does not correlate with strong lensing brings into question the notion that unrelaxed clusters undergoing major mergers are more effective gravitational lenses. In particular, Torri et al. (2004) analyzed two different projections through a single temporally resolved cluster merger and argued that mergers significantly enhance strong lensing cross sections. While individual projections can be enhanced by the presence of significant substructure and similar examples exist for our clusters, these enhancements due to chance alignments of substructures are diluted, in the orientation average, by the other projections for which substructures are not aligned. In addition, Zentner & Bullock (2003) found that the degree of substructure in dark matter halos anti-correlates with concentration, and we have seen that more centrally concentrated clusters tend to dominate the lensing cross section. Finally, our conclusion here that substructure does not correlate with strong

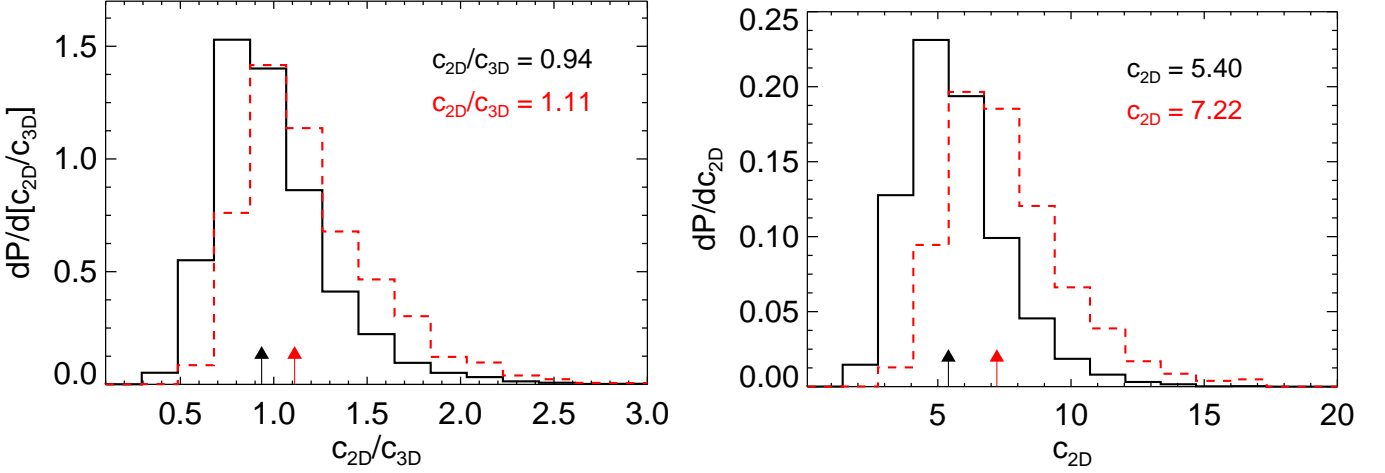


FIG. 12.— *Left*: Lensing (dashed) and total (solid) distributions of the ratio c_{2D}/c_{3D} where the two dimensional concentrations have been measured for each projection through the clusters. Arrows indicate the median of each distribution. Strong lensing prefers the projections through clusters which give $\sim 19\%$ higher concentrations. *Right*: Lensing (dashed) and total (solid) distributions of the two dimensional concentrations, c_{2D} , measured from each projection through the clusters. Arrows indicate the median of the distributions. Cluster lenses have two dimensional concentrations which are 34% higher than the typical cluster in the Universe.

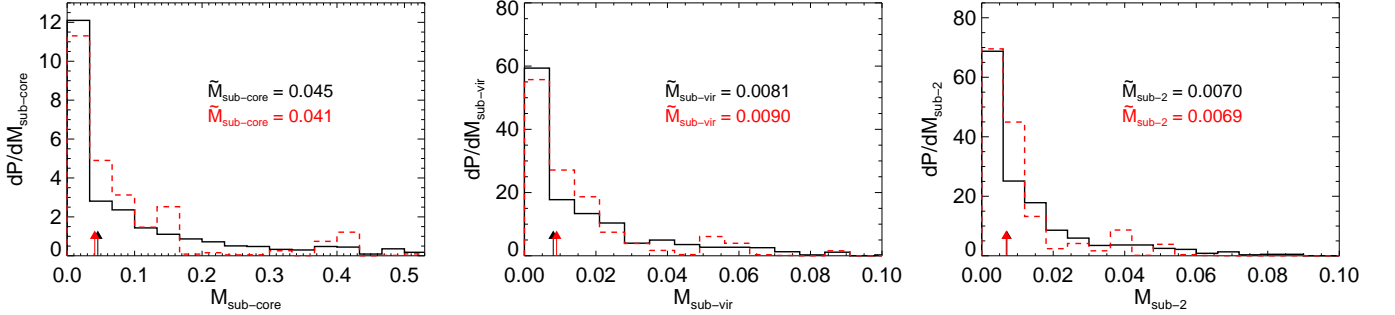


FIG. 13.— Lensing (dashed) and total (solid) distributions of the substructure statistics. The left panel shows the distributions of $M_{\text{sub-core}}$, which is the mass in substructure normalized by the dense core mass. The middle panel shows $M_{\text{sub-vir}}$, which is the mass in substructure normalized by the virial mass. The right panel shows $M_{\text{sub-2}}$, which is ratio of the the single most massive substructure to the virial mass. The median of both the lensing and total distributions, indicated by the arrows, are labeled on each plot. The agreement between the lensing and total distributions for these three different substructure statistics clearly indicates that *the population of cluster lenses are no more relaxed or disturbed than typical clusters in the Universe*.

lensing is reinforced by the results of the no substructure analog halos in § 5. There we saw that smoothly redistributing all the mass in substructure had a marginal effect, $\sim 5 - 10\%$, on the total number of giant arcs produced. Our statistical analysis of 13,594 different orientations of 878 clusters clearly indicates that *the population of cluster lenses are no more relaxed or disturbed than typical clusters in the Universe*.

7. DO THE ARCS DISCOVERED IN THE RCS AGREE WITH Λ CDM?

In this section we revisit the issue of the abundance of giant arcs in the Red Cluster Sequence cluster survey. Gladders et al. (2003) surveyed 90 deg^2 and found several giant arcs, all in clusters at high redshift $z > 0.6$. DHH were unable to determine whether the number of giant arcs discovered in the RCS is consistent with the Λ CDM model because the simulation cube used in that study was too small (but see Wambsganss et al. 2004a). Here we revisit this comparison using a simulation vol-

ume $(320/141.3)^3 = 11.6$ times larger. In Figure 14 we plot the ratio of the RCS volume to the volume of our $320 h^{-1} \text{ Mpc}$ simulation cube as a function of redshift. Our simulation volume is larger than the RCS for $z \sim 0.7$, where three of the five RCS arcs which we consider occur (see below), and comparable to the RCS volume for higher redshifts $0.7 \lesssim z \lesssim 1.0$ where the other two RCS arcs land. Hence, we have a sufficient volume to sample the very rare massive clusters likely to be responsible for the RCS strong lensing (Ho & White 2004).

7.1. The Number Density of Background Galaxies

Gravitational lensing conserves surface brightness but does not conserve total integrated flux. Because arcs are resolved, at least in the tangential direction, arc detection should be limited by surface brightness rather than integrated flux. In the regime where arcs are resolved both tangentially and radially, there is no magnification bias. However, high redshift galaxies are known to be

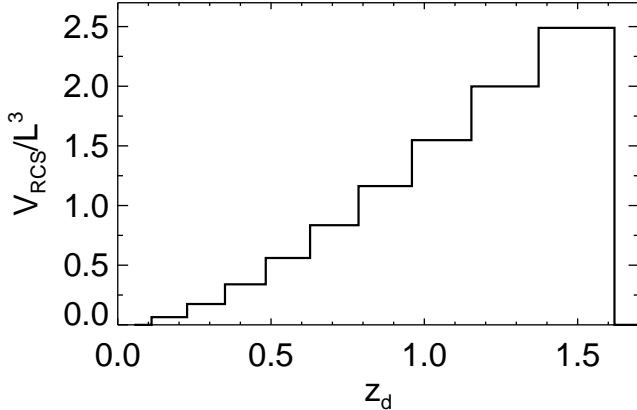


FIG. 14.— The ratio of volume of the 90 deg² RCS survey to our simulation volume as a function of redshift. The quantity (V_j/L^3) is plotted for each snapshot redshift z_j where V_j is given by eqn. (8) and $L = 320 h^{-1}$ Mpc is the size of our simulation cube. The snapshot at redshift z_j , was taken to represent the volume of the Universe over the redshift range $[\frac{z_j+z_{j-1}}{2}, \frac{z_j+z_{j+1}}{2}]$, which is represented by the bins of the histogram.

TABLE 2
DENSITY OF BACKGROUND SOURCES

z_s	$z_{\min} - z_{\max}$	n_{gal}
1.0	0.75 – 1.25	6.25
1.5	1.25 – 1.75	1.67
2.0	1.75 – 2.50	3.96
3.0	2.50 – 3.50	3.54
4.0	3.50 – 5.00	0.62

NOTES—Density of background sources used in this paper.

compact with half light radii $r_h \sim 0.3''$ (Ferguson et al. 2004) and thus giant arcs could be radially unresolved. This depends on both the radial magnification of the lensed image and the resolution or seeing. About half of the arcs published by Gladders et al. (2003) are resolved radially, while the other half are not. For these radially unresolved arcs there is a small amount of magnification bias because the image is integrated over the seeing disk in the radial direction. Because the typical radial magnifications will be small ($\sim \text{seeing}/r_h \sim 2$), we chose to neglect this effect here as it will be negligible compared to our dominant uncertainty, which turns out to be the counts of background galaxies. A more careful analysis could include this radial magnification bias by assuming a typical seeing and including a distribution of source sizes in the Monte Carlo part of the ray tracing simulation (see e.g. Ho & White 2004).

Gladders et al. (2003) impose a surface brightness cut on their arc sample of $\mu_{RC} < 24$. Thus, in order to compare statistics, we require the surface brightness function of high redshift galaxies, rather than the luminosity function. Note that because the size distribution of galaxies is broad (Ferguson et al. 2004) and the luminosities and sizes of high redshift galaxies are correlated (Bouwens et al. 2004; Trujillo et al. 2004), simply using the mean size to convert a limiting surface brightness to a limiting magnitude will not give the correct number

counts.

Fontana et al. (2000) publish a photometric redshift catalog which includes the New Technology Telescope (NTT) Deep Field. Poli et al. (1999) measured the half light radii of all the galaxies in the NTT deep field using image deconvolution techniques. The area of the NTT deep field is only 4.8 arcmin². Even for the relatively coarse redshift bins we use here $\Delta z \sim 1.0$, cosmic variance for such a small field can be as large as $\sim 50\%$ (Somerville et al. 2004). Furthermore, half light radii measured from space based imaging would be clearly preferable to deconvolved ground based data. However, no wide field space based catalog which includes redshifts and galaxy sizes exists at the time of writing. Thus, we use the Poli et al. (1999) sizes with the Fontana et al. (2000) photo- z 's to determine the number of background galaxies in each redshift bin with $\mu_R < 24$. The density of background sources used for each source redshift bin are listed in Table 2. We caution that uncertainty in the density of sources is likely to be a significant source of error in our comparison of the abundance of giant arcs to theory. For example, the NTT deep field contains 23 galaxies in the redshift range [2.5,3.5] with $R < 25$, or 4.8 galaxies per arcmin⁻². Yet the incompleteness corrected luminosity function derived from the $z \sim 3$ Lyman break galaxy sample of Steidel et al. (1999) predicts 1.9 galaxies per arcmin⁻² in this range.

7.2. Comparison with RCS

The cumulative distribution of image splittings predicted for the RCS survey from our ray tracing simulations with BCGs added is shown in the left panel of Figure 15. Contributions from the individual source planes are also shown, along with the total number predicted from dark matter alone. BCGs significantly increase the total number of arcs for separations $\theta \lesssim 15''$ consistent with previous results (DHH; Meneghetti, Bartelmann, & Moscardini 2003b; Ho & White 2004).

We restrict our comparison to giant arcs with separations $\theta > 10''$, since for smaller separations, our results will be very sensitive to the details of how we paint BCGs onto dark halos. We also restrict attention to arcs with length to width ratios $L/W \gtrsim 10$. Five of the arcs from Table 1 of Gladders et al. (2003) satisfy these criteria. These are the two arcs in RCS 0224.5-0002 ($z = 0.77$), one arc in RCS 1324.5+28245 ($z = 0.85$), one arc in RCS 1419.2+5326 ($z = 0.64$), and one of the arcs in the secondary high redshift sample RCS 2319.9+0038 ($z = 0.91$; Gladders private communication January 2005).

The right panel of Figure 15 compares the predicted redshift histogram of arcs with $\theta > 10''$ to the redshift histogram of the RCS lensing clusters using the same binning. It is rather surprising that the RCS did not detect any arcs with $z < 0.63$, as the simulations predict ~ 5 arcs in this redshift range. For redshifts $z > 0.63$, the simulations predict ~ 4 arcs, whereas all five of the RCS arcs are in this range. Although it is odd that the RCS arcs all pile up between $z = 0.6 - 0.9$, this anomaly is not statistically significant considering the small numbers of objects. We conclude that, at present, there is no significant excess of high redshift lensing clusters in the RCS survey.

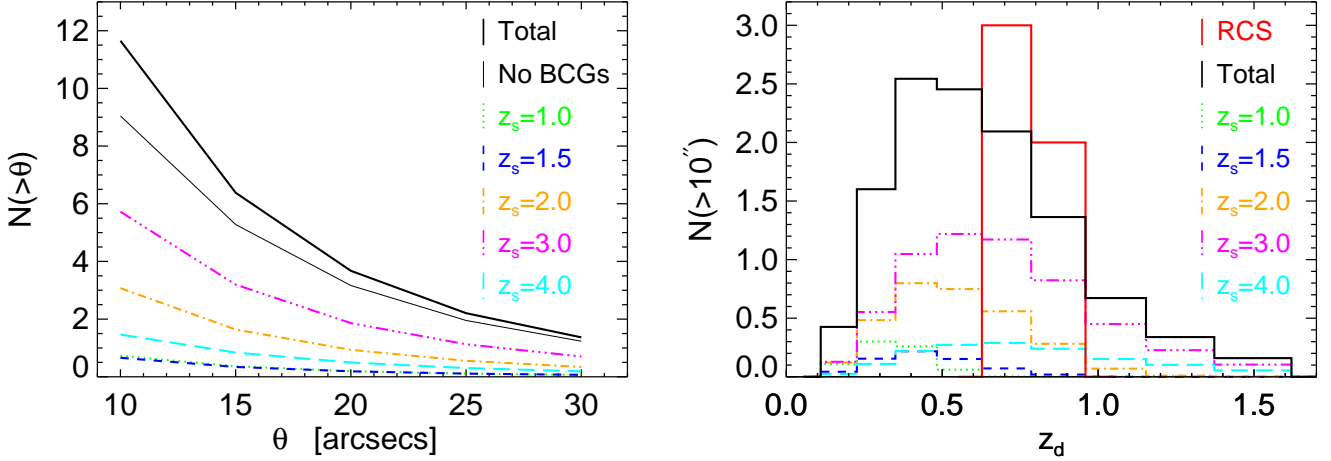


FIG. 15.— *Left:* Predicted cumulative distribution of giant arc separations for the RCS cluster survey. The green (dotted), blue (short-dashed), orange (dot-dashed), magenta (dot-dot-dashed), and cyan (long dashed) curves are the individual contributions from the source planes at $z_s = 1.0, 1.5, 2.0, 3.0$, and 4.0 , respectively. The sum of these curves gives the total number of multiply imaged quasars which is the thick black (solid) curve. The thin solid (black) line shows the total number of lenses if BCGs are neglected and we ray trace through dark matter only. *Right:* Redshift histogram of cluster lenses with splittings $\theta > 10''$ in the RCS survey. The individual contributions from each source plane are also plotted with the same line and color scheme as in the left panel. The thick black (solid) histogram is the total number of giant arcs predicted including BCGs. The red (solid) histogram is the observed redshift distribution of cluster lenses in the RCS from Gladders et al. (2003).

Before we conclude this section, we compare the predicted number of arcs here to the previous results in DHH. They predicted a total of ~ 3 arcs in the RCS for $z < 1.0$, whereas here we predict ~ 8 arcs in this redshift range. First, the cosmological parameters for the simulations used in that study were slightly different, most importantly the simulation used by DHH had $\sigma_8 = 0.9$, whereas that used in this study used $\sigma_8 = 0.95$. This changes the abundance $N(>M)$ of massive clusters by $\sim 35 - 40\%$ for $M = 3 \times 10^{14} h^{-1} M_\odot$ and as much as $\sim 170\%$ for $M = 3 \times 10^{15} h^{-1} M_\odot$ at $z \sim 0.5$. Although significant, the change in cluster abundance does not account for the entire disagreement. Another difference which could be important for the higher redshift ($z \gtrsim 0.6$) clusters is the additional high redshift source planes ($z_s = 3.0$ and $z_s = 4.0$) used here, whereas the highest redshift source plane considered by DHH was $z_s = 2.0$. However, it is likely that the factor of 11.6 smaller volume used in that study is responsible for most of the discrepancy. As indicated by Figure 7, the mass function is a very steep function of cluster mass and furthermore the scatter about this mean relation is large because of the large underlying scatter in cluster properties (i.e. Figure 8). Large cosmological volumes are thus required before convergence to the cosmic mean can be achieved.

Have the results of this study converged to the correct cosmic mean lensing cross sections? First note that the small volume simulated is at least partly compensated by averaging over a large number of orientations for each cluster. Although the lensing distribution of cluster masses in the right panel of Figure 7 indicates that halos $M \sim 5 \times 10^{14} h^{-1} M_\odot$ are dominating the total lensing cross section, the tail of this distribution suggests that we may not yet have converged at the high mass end. Possible evidence for a lack of convergence is the fact

that Li et al. (2005) find much lower optical depths for a simulation volume of similar size. Besides convergence to the mean, another serious issue is cosmic variance. Since the volume we simulated is comparable to the volume of the RCS, how likely are these two realizations to give the same answer? Answering this question requires one to measure the highly non-Gaussian probability distributions of very rare events. This is clearly beyond the scope of the present study, yet it is a question which must be tackled if giant arc statistics are to become a quantitative tool for cosmology.

8. SUMMARY AND CONCLUSIONS

We attempted to isolate which properties of CDM clusters make them effective gravitational lenses, by introducing several different types of ‘Analog Halos,’ which retain one or more of the properties of the real simulated clusters. The results of this analysis are:

- Spherical halos underpredict the abundance of giant arcs by a factor as large as 50 and triaxial models fall short by a factor as much as 60% (see Table 1).
- Triaxiality increases the number of giant arcs by a factor of 4-25 compared to the spherically symmetric halos, because the shallow density cusps $\rho \propto r^{-1}$ of CDM halos result in an extreme sensitivity to triaxiality (DHH; Dalal & Keeton 2003; Bartelmann & Meneghetti 2004).
- Projections of halo substructure onto small radii and the large scale mass distribution of clusters do not significantly influence strong lensing cross sections. The number of giant arcs produced by CDM halos is primarily determined by the mass distribution with a mean overdensity of $\sim 10,000$.

- The clumpy cores of dark matter halos result in $\sim 25 - 60\%$ more giant arcs than smooth ellipsoids, which suggests that the abundance of giant arcs can probe the small scale morphology of dark matter halos.

We measured the properties of a large ensemble of clusters and characterized the cluster lens population by computing cross sections for each cluster with ray tracing simulations. Our statistical comparison of the properties of the lensing and total cluster populations yielded the following results:

- NFW profiles provide just as good a fit to lensing clusters as they do to the total population of clusters.
- The typical mass of a lensing cluster is $M_{\text{vir}} = 4.5 \times 10^{14} h^{-1} M_{\odot}$.
- Lensing clusters have 34% higher concentrations than the typical cluster at the same redshift with a similar mass. This bias is result of a combination of two effects. First, the lensing population is biased towards clusters with higher three dimensional concentrations. Second, given a three dimensional concentration, orientation bias will favor projections along the major axis with higher two dimensional concentrations.
- The anomalously high concentrations $c > 14$ recently reported by several groups (Kneib et al. 2003; Gavazzi et al. 2003; Broadhurst et al. 2005b) appear inconsistent with the concentration distribution in our simulations, which predict that $< 2\%$ of lensing clusters should have concentrations this high.
- The population of cluster lenses are no more relaxed or disturbed than typical clusters in the Universe.
- Strong lensing clusters tend to have their principal axis aligned with the the line of sight. The median angle is $|\cos \theta| = 0.67$.
- The distribution of axis ratios of strong lensing clusters is indistinguishable from the total cluster population.

We revisited the question of whether there is an excess of giant arcs detected for high redshift clusters in the RCS survey (Gladders et al. 2003). Our simulations predict 9 total arcs in the RCS survey, whereas five were

discovered. At low redshift ($z \lesssim 0.6$) the RCS found zero arcs, which is discrepant with our prediction of ~ 5 . At high redshift ($z \gtrsim 0.6$), our prediction of ~ 4 giant arcs is consistent with the five discovered in the RCS. There is no significant excess of high redshift lensing clusters in the RCS survey over predictions from the Λ CDM model.

Finally, we emphasize that the results in this work were all based on dissipationless dark matter only N-body simulations. Thus, we implicitly assumed that dissipative baryonic processes such as heating, cooling, turbulence, and star formation have a negligible effect on the average surface mass density of a cluster within $r_{10,000} \sim 300 h^{-1} \text{ kpc}$ (although we did account for the effect of brightest cluster galaxies in § 3.1). While hydrodynamical simulations of cluster formation are making rapid progress (Gnedin et al. 2004; Kazantzidis et al. 2004; Kravtsov et al. 2005), they are not yet mature enough to make definitive predictions about the effects on the mass distribution on scales relevant for strong lensing (Puchwein et al. 2005). This is a fruitful topic for future research, considering the potentially significant impact these processes could have on our interpretation of strong lensing in clusters.

We acknowledge helpful discussions with Olivier Dore, Shirley Ho, David Hogg, Mike Gladders, Peter Schneider, Risa Wechsler, and Joachim Wambsganss. Jeffrey Newman and Alice Shapley helped us with the number counts of galaxies, and Yeong-Shang Loh pointed us to relevant references on BCGs. We thank Joanne Cohn and Martin White for reading an early version of this manuscript and providing helpful comments. JFH would like to thank his thesis advisors David Spergel and Michael Strauss for advice and guidance during his time in Princeton, where this work was begun. For part of this study JFH was supported by Proctor Graduate fellowship at Princeton University and by a generous gift from the Paul & Daisy Soros Fellowship for New Americans. The program is not responsible for the views expressed. JFH and ND are supported by NASA through Hubble Fellowship grants # 01172.01-A and 01148.01-A respectively, awarded by the Space Telescope Science Institute, which is operated by the Association of Universities for Research in Astronomy, Inc., for NASA, under contract NAS 5-26555. Computer time was provided by the National Computational Science Alliance under program #MCA04N002P, and some computations were performed on the NSF Terascale Computing System at the Pittsburgh Supercomputing Center. The ray tracing simulations used computational facilities at Princeton supported by NSF grant AST-0216105.

REFERENCES

- Allgood, B et al. 2005, in preparation
 Arabadjis, J. S., Bautz, M. W., & Garmire, G. P. 2002, *ApJ*, 572, 66
 Barnes, J. & Efstathiou, G. 1987, *ApJ*, 319, 575
 Bartelmann, M. & Weiss, A. 1994, *A&A*, 287, 1
 Bartelmann, M., Steinmetz, M., & Weiss, A. 1995, *A&A*, 297, 1
 Bartelmann, M. 1995, *A&A*, 303, 643
 Bartelmann, M. 1996, *A&A*, 313, 697
 Bartelmann, M., Huss, A., Colberg, J. M., Jenkins, A., & Pearce, F. R. 1998, *A&A*, 330, 1
 Bartelmann, M., Meneghetti, M., Perrotta, F., Baccigalupi, C., & Moscardini, L. 2003, *A&A*, 409, 449
 Bartelmann, M. & Meneghetti, M. 2004, *A&A*, 418, 413
 Bode, P. & Ostriker, J. P. 2003, *ApJS*, 145, 1
 Bouwens, R. J., Illingworth, G. D., Blakeslee, J. P., Broadhurst, T. J., & Franx, M. 2004, *ApJ*, 611, L1
 Broadhurst, T., et al. 2005, *ApJ*, 621, 53
 Broadhurst, T., Takada, M., Umetsu, K., Kong, X., Arimoto, N., Chiba, M., & Futamase, T. 2005, *ApJ*, 619, L143
 Bryan, G. L. & Norman, M. L. 1998, *ApJ*, 495, 80

- Bullock, J. S., Kolatt, T. S., Sigad, Y., Somerville, R. S., Kravtsov, A. V., Klypin, A. A., Primack, J. R., & Dekel, A. 2001, *MNRAS*, 321, 559
- Carlstrom, J. E., Holder, G. P., & Reese, E. D., *ARA&A*, 40, 643
- Dalal, N. & Keeton, C. R. 2003, *ArXiv Astrophysics e-prints*, astro-ph/0312072
- Dalal, N., Holder, G., & Hennawi, J. F. 2004, *ApJ*, 609, 5
- Dalal, N., Hennawi, J. F., & Bode, P. 2005, *ApJ*, 622, 99
- Davis, M., Efstathiou, G., Frenk, C. S., & White, S. D. M. 1985, *ApJ*, 292, 371
- De Lucia, G., Kauffmann, G., Springel, V., White, S. D. M., Lanzoni, B., Stoehr, F., Tormen, G., & Yoshida, N. 2004, *MNRAS*, 348, 333
- Ebeling, H., Edge, A. C., & Henry, J. P. 2001, *ApJ*, 553, 668
- Edge, A. C. & Stewart, G. C. 1991, *MNRAS*, 252, 428
- Ettori, S., Fabian, A. C., Allen, S. W., & Johnstone, R. M. 2002, *MNRAS*, 331, 635
- Faber, S. M. & Jackson, R. E. 1976, *ApJ*, 204, 668
- Fan, X., et al. 2001, *AJ*, 121, 54
- Ferguson, H. C., et al. 2004, *ApJ*, 600, L107
- Fisher, D., Illingworth, G., & Franx, M. 1995, *ApJ*, 438, 539
- Flores, R. A., Maller, A. H., & Primack, J. R. 2000, *ApJ*, 535, 55
- Fontana, A., D'Odorico, S., Poli, F., Giallongo, E., Arnouts, S., Cristiani, S., Moorwood, A., & Saracco, P. 2000, *AJ*, 120, 2206
- Gavazzi, R., Fort, B., Mellier, Y., Pelló, R., & Dantel-Fort, M. 2003, *A&A*, 403, 11
- Gnedin, O. Y., Kravtsov, A. V., Klypin, A. A., & Nagai, D. 2004, *ApJ*, 616, 16
- Gill, S. P. D., Knebe, A., & Gibson, B. K. 2004, *ArXiv Astrophysics e-prints*, astro-ph/0404258
- Gladders, M. D., Hoekstra, H., Yee, H. K. C., Hall, P. B., & Barrientos, L. F. 2003, *ApJ*, 593, 48
- Gladders, M. D., & Yee, H. K. C. 2004, *ArXiv Astrophysics e-prints*, astro-ph/0411075
- Schulz, A. E. et al. 2005, in preparation
- Ho, S., & White, M. 2004, *ArXiv Astrophysics e-prints*, astro-ph/0408245
- Hockney, R. W. & Eastwood, J. W. 1981, *Computer Simulation Using Particles*, New York: McGraw-Hill, 1981
- Hogg, D. W., Baldry, I. K., Blanton, M. R., Eisenstein, D. J. 2002, *ArXiv Astrophysics e-prints*, astro-ph/0210394
- Hu, W. & Kravtsov, A. V. 2003, *ApJ*, 584, 702
- Jenkins, A., Frenk, C. S., White, S. D. M., Colberg, J. M., Cole, S., Evrard, A. E., Couchman, H. M. P., & Yoshida, N. 2001, *MNRAS*, 321, 372
- Jing, Y. P. & Suto, Y. 2002, *ApJ*, 574, 538
- Kazantzidis, S., Kravtsov, A. V., Zentner, A. R., Allgood, B., Nagai, D., & Moore, B. 2004, *ApJ*, 611, L73
- Kelson, D. D., Zabludoff, A. I., Williams, K. A., Trager, S. C., Mulchaey, J. S., & Bolte, M. 2002, *ApJ*, 576, 720
- Kneib, J., et al. 2003, *ApJ*, 598, 804
- Kochanek, C. S., et al. 2000, *ApJ*, 543, 131
- Kosowsky, A. 2003, *New Astronomy Review*, 47, 939
- Kravtsov, A. V., et al. 2003, *ArXiv Astrophysics e-prints*, astro-ph/0308519
- Kravtsov, A. V., Nagai, D., & Vikhlinin, A. A. 2005, *ArXiv Astrophysics e-prints*, arXiv:astro-ph/0501227
- Lacey, C., & Cole, S. 1994, *MNRAS*, 271, 676
- Lewis, A. D., Buote, D. A., & Stocke, J. T. 2003, *ApJ*, 586, 135
- Li, G. L., Mao, S., Jing, Y. P., Bartelmann, M., Kang, X., & Meneghetti, M. 2005, *ArXiv Astrophysics e-prints*, astro-ph/0503172
- Luppino, G. A., Gioia, I. M., Hammer, F., Le Fèvre, O., & Annis, J. A. 1999, *A&AS*, 136, 117
- Meneghetti, M., Bolzonella, M., Bartelmann, M., Moscardini, L., & Tormen, G. 2000, *MNRAS*, 314, 338
- Meneghetti, M., Bartelmann, M., & Moscardini, L. 2003, *MNRAS*, 340, 105
- Meneghetti, M., Bartelmann, M., & Moscardini, L. 2003, *MNRAS*, 346, 67
- Meneghetti, M., Bartelmann, M., Dolag, K., Moscardini, L., Perrotta, F., Baccigalupi, C., & Tormen, G. 2004, *ArXiv Astrophysics e-prints*, astro-ph/0405070
- Miralda-Escude, J. 1995, *ApJ*, 438, 514
- Natarajan, P. & Kneib, J. 1996, *MNRAS*, 283, 1031
- Navarro, J. F., Frenk, C. S., & White, S. D. M. 1997, *ApJ*, 490, 493
- Oegerle, W. R. & Hoessel, J. G. 1991, *ApJ*, 375, 15
- Oguri, M., Lee, J., & Suto, Y. 2003, *ApJ*, 599, 7
- Oguri, M., et al. 2004, *ApJ*, 605, 78
- Oguri, M. & Keeton, C. R. 2004, *ArXiv Astrophysics e-prints*, astro-ph/0403633
- Oguri, M., & Lee, J. 2004, *MNRAS*, 355, 120
- Phillips, P. M., et al. 2001, *MNRAS*, 328, 1001
- Poli, F., Giallongo, E., Menci, N., D'Odorico, S., & Fontana, A. 1999, *ApJ*, 527, 662
- Power, C., Navarro, J. F., Jenkins, A., Frenk, C. S., White, S. D. M., Springel, V., Stadel, J., & Quinn, T. 2003, *MNRAS*, 338, 14
- Puchwein, E., Bartelmann, M., Dolag, K., & Meneghetti, M. 2005, *ArXiv Astrophysics e-prints*, arXiv:astro-ph/0504206
- Richards, G. T., et al. 2001, *AJ*, 121, 2308
- Richards, G. T., Nichol, R. C., Gray, A. G., Brunner, R. J., Lupton, R. H., & Vanden Berk, D. E. 2003, *American Astronomical Society Meeting*, 203
- Romer, A. K., Viana, P. T. P., Liddle, A. R., & Mann, R. G. 2001, *ApJ*, 547, 594
- Sand, D. J., Treu, T., Smith, G. P., & Ellis, R. S. 2004, *ApJ*, 604, 88
- Sand, D. J., Treu, T., Ellis, R. S., & Smith, G. P. 2005, *ArXiv Astrophysics e-prints*, arXiv:astro-ph/0502528
- Schneider, P., Ehlers, J., & Falco, E. E. 1992, *Gravitational Lenses*, XIV, 560 pp. 112 figs.. Springer-Verlag Berlin Heidelberg New York. Also *Astronomy and Astrophysics Library*
- Schwan, D., et al. 2003, *New Astronomy Review*, 47, 933
- Sheth, R. K. 2003, *MNRAS*, 345, 1200
- Sheth, R. K., & Jain, B. 2003, *MNRAS*, 345, 529
- Smith, G. P., Kneib, J., Ebeling, H., Czoske, O., & Smail, I. 2001, *ApJ*, 552, 493
- Somerville, R. S., Lee, K., Ferguson, H. C., Gardner, J. P., Moustakas, L. A., & Giavalisco, M. 2004, *ApJ*, 600, L171
- Spergel, D. N., et al. 2003, *ApJS*, 148, 175
- Steidel, C. C., Adelberger, K. L., Giavalisco, M., Dickinson, M., & Pettini, M. 1999, *ApJ*, 519, 1
- Torri, E., Meneghetti, M., Bartelmann, M., Moscardini, L., Rasia, E., & Tormen, G. 2004, *MNRAS*, 349, 476
- Trujillo, I., et al. 2004, *ApJ*, 604, 521
- Tyson, J. A., Kochanski, G. P., & dell'Antonio, I. P. 1998, *ApJ*, 498, L107
- Vanden Berk, D. E., et al. 2001, *AJ*, 122, 549
- Warren, M. S., Quinn, P. J., Salmon, J. K., & Zurek, W. H. 1992, *ApJ*, 399, 405
- Wambsganss, J., Bode, P., & Ostriker, J. P. 2004, *ApJ*, 606, L93
- Wambsganss, J., Bode, P., & Ostriker, J. P. 2004, *ArXiv Astrophysics e-prints*, astro-ph/0405147
- Wechsler, R. H., Bullock, J. S., Primack, J. R., Kravtsov, A. V., & Dekel, A. 2002, *ApJ*, 568, 52
- Weller, J., Ostriker, J. P., & Bode, P. 2004, *ArXiv Astrophysics e-prints*, astro-ph/0405445
- White, M. 2001, *A&A*, 367, 27
- Wright, C. O., & Brainerd, T. G. 2000, *ApJ*, 534, 34
- Zhdanov, V. I. & Surdej, J. 2001, *A&A*, 372, 1
- Zentner, A. R., & Bullock, J. S. 2003, *ApJ*, 598, 49